

Fluid dynamics of oscillatory flow in three-dimensional branching networks ^{EP}

Cite as: Phys. Fluids **31**, 063601 (2019); <https://doi.org/10.1063/1.5093724>

Submitted: 24 February 2019 . Accepted: 08 May 2019 . Published Online: 03 June 2019

Kaustav Pradhan , and Abhijit Guha

COLLECTIONS

 This paper was selected as an Editor's Pick



View Online



Export Citation



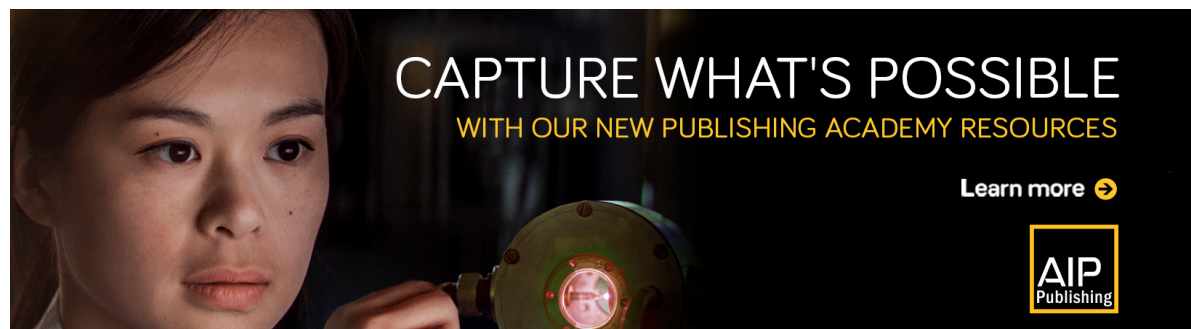
CrossMark

ARTICLES YOU MAY BE INTERESTED IN


[Numerical study of thermocapillary migration of a bubble in a channel with an obstruction](#)
Physics of Fluids **31**, 062101 (2019); <https://doi.org/10.1063/1.5094033>



[Bowling water drops on water surface](#)
Physics of Fluids **31**, 067101 (2019); <https://doi.org/10.1063/1.5096235>

[Passive vortical flows enhance mass transport in the interior of a coral colony](#)
Physics of Fluids **31**, 061701 (2019); <https://doi.org/10.1063/1.5094076>



CAPTURE WHAT'S POSSIBLE
WITH OUR NEW PUBLISHING ACADEMY RESOURCES

Learn more 



Fluid dynamics of oscillatory flow in three-dimensional branching networks

Cite as: Phys. Fluids 31, 063601 (2019); doi: 10.1063/1.5093724

Submitted: 24 February 2019 • Accepted: 8 May 2019 •

Published Online: 3 June 2019



View Online



Export Citation



CrossMark

Kaustav Pradhan  and Abhijit Guha^{a)}

AFFILIATIONS

Mechanical Engineering Department, Indian Institute of Technology Kharagpur, Kharagpur 721302, India

^{a)} Author to whom correspondence should be addressed: a.guha@mech.iitkgp.ac.in

ABSTRACT

The present study is aimed at understanding and thoroughly documenting the complex unsteady fluid dynamics in six generations of a model human bronchial tree, comprising 63 straight sections and 31 bifurcation modules, during a complete breathing cycle. The computational task is challenging since the complexity of an elaborate network is augmented with adopted stringent criteria for spatial and temporal accuracy and convergence at each time step (10^{-8} for each scaled residual). The physical understanding of the fluid dynamics of steady expiratory flow is taken to a similar level of fine details that have been previously established for steady inspiratory flow in earlier publications of the authors. The effects of three-dimensional arrangement of the same branches on the oscillatory flow structure are determined. It is found that the quasisteady assumption is approximately valid in the neighborhood of the peak flow rate, both during inspiration and expiration. Unsteady effects are at their maximum during the changeover from expiration to inspiration and inspiration to expiration. At these time instants, regions of bidirectional flow are observed in all branches with significant secondary motion at various cross sections (none of these features can be predicted by steady state simulations). It is described how the symmetry of the solution with respect to both space and time—found in the oscillating, fully developed flow in a pipe—are destroyed in the unsteady effects that occur in the oscillating flow in a branching network. As the Womersley number is increased, the unsteady effects at all branches increase, and bidirectional flow exists over a greater portion of a cycle. The flow division at a bifurcation module during inspiratory flow generates large asymmetry in the flow field with nonuniform mass flow distribution among the branches of a generation (even in a geometrically symmetric network), whereas flow combination at the same bifurcation module during expiratory flow tends to produce more symmetry in the flow field, displaying essential irreversibility of fluid dynamics.

Published under license by AIP Publishing. <https://doi.org/10.1063/1.5093724>

I. INTRODUCTION

The process of breathing is an unsteady flow phenomenon involving periodic reversal of the predominant flow direction. A single breathing cycle comprises an inhalation/inspiratory phase during which air is drawn into the respiratory system and an exhalation/expiratory phase during which air is released to the surroundings. The present study aims to develop a physical understanding of the complex fluid dynamic changes that occur in the human bronchial network during a breathing cycle. Such a study requires careful numerical simulation of temporally oscillating flow in the intricate three-dimensional flow passages of the bronchial tree.

There are many studies on the flow in bifurcating networks representing the human bronchial tree, which consider the flow to be steady (or quasisteady). In two recent publications,^{1,2}

the flow in three-dimensional branching networks comprising six generations of branches was comprehensively analyzed, specifying and systematizing the complex primary flow field, and quantifying the generation and evolution of secondary motion. Zhao and Lieber^{3,4} performed comprehensive experiments to study the velocity profiles obtained in a single bifurcation for both steady inspiratory and expiratory flows. Correlations for the pressure loss across a model bifurcation were proposed by Kang *et al.*⁵ They found that the pressure loss coefficient shows a power-law dependence on the Reynolds number and the length-to-diameter ratio, and a very weak dependence on the bifurcation angle. Comer *et al.*⁶ studied the air flow in symmetric branching networks comprising three generations. Wilquem and Degrez⁷ performed a two-dimensional study of the flow in three generations of human airways. They concluded that the nonuniform flow distribution in the network rendered

a resistance model of flow partitioning (based on Kirchoff's law) inadequate. Zhang *et al.*⁸ considered the flow in a symmetric triple bifurcation network. Recently, studies of fluid flow and particle deposition have been performed in patient-specific models developed from computed tomography (CT) imaging data^{9–11} and in computer generated asymmetric lung models.^{12,13} However, such studies apply to specific individuals, and thus, generalized geometric models are normally used in studies where understanding general fluid dynamic features is the priority.

It is important to realize that apparent symmetry in the geometry of any two branches does not automatically imply symmetry in the flow field in those two branches. The combined effects of flow path curvature in the bifurcation module, flow division at a bifurcation, and inertia of the flow result in skewed velocity profiles (with maximum velocity near the inner edge of bifurcation) in the daughter branches even when the velocity field in the mother branch is symmetric about the bifurcation ridge between that mother and its daughter branches. Viscous effects try to establish a circumferentially symmetric paraboloidal velocity profile in the straight portion of a branch but usually its length is insufficient for the complete removal of asymmetry, and the flow encounters the next bifurcation module where further asymmetry is introduced. Thus, even though each bifurcation appears to divide into two geometrically similar branches, the flow distribution is nonuniform. A detailed explanation and results are given in Ref. 1.

In comparison to the volume of available literature on theoretical and experimental studies of the steady flow in a branching network, the available literature on the unsteady/oscillatory flow is sparse. Although the steady flow results help to understand the effects of the branching geometry, the study of temporally oscillating flow in the human airways is interesting from the point of view of fundamental fluid dynamics as well as imperative for understanding the transport and deposition of particles in the respiratory tract. The knowledge of particle transport is, in turn, important for understanding the causation of certain diseases and for targeted drug delivery. (A lucid but comprehensive description of the flow of fluid and particles in the human bronchial tree is given by Guha.¹⁴)

Before embarking upon a study of oscillating flow in elaborate branching networks, it is important to acknowledge the known knowledge regarding oscillating flow in a pipe. Sexl¹⁵ gave an analytical solution for the oscillating flow in a pipe following the experimental measurements of cross-sectional velocity distributions by Richardson and Tyler.¹⁶ Lambosy¹⁷ derived an analytical expression for the velocity profile considering a sinusoidal pressure variation across a pipe and gave relations for determining the friction forces. Later, Womersley^{18,19} showed that the interaction between inertial and viscous effects in oscillatory pipe flow would alter the velocity profile such that it would not remain parabolic as in steady laminar flow. Moreover, he showed that a phase-lag developed between the motion of the fluid and the driving pressure gradient. Ray and Durst²⁰ developed semianalytical solutions for laminar fully developed pulsating flow through ducts of arbitrary cross sections. Recently, there have been studies on oscillatory pipe flows considering enhancement of axial heat transfer,²¹ design of novel vortex flow meters,²² and the flow of rarefied gases in rectangular ducts.²³

The theories of Sexl,¹⁵ Lambosy,¹⁷ and Womersley¹⁸ assume that the velocity vectors are aligned to the axis, there is no variation in velocity in the axial direction (fully developed) and the flow field is axisymmetric. Velocity at any instant is then a function of radius alone. Analytical solution for such an unsteady flow is possible. Although certain flow features such as the presence of bidirectional flow in the neighbourhoods of changeover from inspiration to expiration (and vice versa) and the existence of phase difference between velocity and pressure oscillations are common, it is established in the present work that the oscillating flow in a branching network is much more complex. The flow field is developing and nonaxisymmetric, and, is a function of all three space coordinates and time. The presence of flow division (or combination), flow path curvature and inertia give rise to complex variation of flow field, including the presence of strong secondary motion. Present computations show that there may be bidirectional flow in some branches even at the instant of peak expiration and the symmetry between the inspiratory and expiratory phases (that is present in the pipe solution) is lost.

Since the geometric complexity of branching networks renders an analytical solution nearly impossible, the oscillatory flow in such networks has been studied mostly through experiments and numerical simulations. The oscillatory flow in a model bifurcation was studied by Jan *et al.*²⁴ using an order-of-magnitude analysis and flow visualizations. They developed a flow regime map in which three regimes were classified, viz., viscous-dominated, convective acceleration-dominated, and unsteady effects-dominated. Menon *et al.*²⁵ performed experiments for oscillatory flow in models of the human central airway bifurcations. Their results showed that for small frequencies of the oscillations, the velocity profiles in unsteady flow are greatly influenced by the geometry of the bifurcation, and the velocity profiles at peak flow rates resemble the steady flow profiles at comparable Reynolds numbers. Lieber and Zhao²⁶ experimentally studied the flow in a symmetric bifurcation model under oscillatory flow conditions, and reported that the quasisteady assumption is valid only in the vicinity of peak inspiration and peak expiration. Fresconi and Prasad²⁷ experimentally investigated the unsteady secondary flow field during inspiration and expiration in a four-generation branching network. Evgren *et al.*²⁸ performed numerical simulations for the unsteady flow in a 90° bifurcation and studied the secondary flow in the daughter branches in great details. Soni and Thompson²⁹ investigated the effects of temporally varying inlet flow conditions on the flow field in small bronchial tubes, their study being limited to only a few branches. Zhang and Kleinstreuer³⁰ numerically studied the oscillating laminar flow in a symmetric triple bifurcation network. Adler and Brucker³¹ performed experiments to study the oscillatory flow in a realistic model of the upper human airways. Nagels and Cater³² performed large eddy simulations of high frequency oscillating flow in an asymmetric airway model. Recently, studies have been performed to analyze the partitioning of red blood cells at a bifurcation using direct numerical simulations³³ and to determine local viscosity distributions in bifurcating blood flows.³⁴ The above-mentioned previous studies considered rigid wall of the tubes and the flow downstream of the trachea (i.e., did not involve the effects of any geometrical complexity upstream of the trachea). The same spirit of keeping the discussion focused is maintained here.

The present computational study attempts to capture the complex fluid dynamics associated with the oscillatory flow in three-dimensional branching networks, involving periodic reversal of the flow direction, through accurate unsteady simulations of the flow field (with experimental validation of both steady and unsteady computational results). For generalization of the results, dimensions of branches are selected according to the first six generations of a symmetric model of the human bronchial tree,³⁵ comprising 63 straight sections and 31 bifurcation modules. The effects of three-dimensional arrangement of the same branches on the flow structures occurring at various time instants of a breathing cycle are systematically studied here by considering both in-plane and out-of-plane configurations of branches. The flow field is asymmetric even in a geometrically symmetric network, and hence all branches of the six generations are included in the computation, with appropriate meshes for the three-dimensionally complex internal passages. The computational task of generating (and analyzing) unsteady flow is challenging since the complexity of such an elaborate network is augmented with adopted stringent criteria for spatial and temporal accuracy (with double precision arithmetic) and convergence at each time step (10^{-8} for each scaled residual) with 14×10^6 computational cells, 500 time steps within a cycle and about 500 h of computation time per cycle on parallelized four i-5 processors. Two cycles are simulated for each set of geometry and flow parameters; three such complete simulations are reported in the present work (in-plane at $\alpha = 2.64$, out-of-plane at $\alpha = 2.64$, and in-plane at $\alpha = 10$, α being the Womersley number, thus totalling about 3000 h of computation time). Spatial and temporal accuracy of the solutions is demonstrated by comparing them with experimental results, and this makes it possible to draw dependable physical conclusions from the simulations presented. With the help of velocity contours and vector plots of the primary and secondary flow, a qualitative and quantitative study is performed on the temporal and spatial evolution of flow during a breathing cycle. It is shown that significant flow asymmetry exists throughout the network during the inspiratory phase, whereas the flow during the expiratory phase is characterized by a much smaller level of asymmetry. Although computations are carried out here for a model bronchial tree, the conclusions and physical understanding emanating from this study are also applicable to oscillating flow in a future engineered branching network.

There are at least three aspects of this study which are distinctive. First of all, the physical understanding of the fluid dynamics of steady expiratory flow through an elaborate branching network is taken to a similar level of fine details that have been previously established for steady inspiratory flow in Refs. 1 and 2. Second, the unsteady effects during both inspiration and expiration in an elaborate network are explored, relating to the known physics of unsteady effects exhibited by fully developed flow in a single pipe established through the theoretical work of Sexl,¹⁵ Lambossy,¹⁷ and Womersley.¹⁸ The manifestation of the unsteady effect may be appreciated in several ways. As an example, the unsteady effect may be quantified in terms of the difference of the actual unsteady solution at a particular instant and the steady solution computed with the same boundary conditions at that instant. (For example, at the instants $t = 0$, $t = T/2$, or $t = T$ of a breathing cycle, steady computations would give no flow in the entire network, but the unsteady computations give rise to oppositely directed regions of flow at

various cross sections of the network.) The unsteady effects may also be appreciated by quantifying the difference of the unsteady flow solution at a particular location of the network at a time instant of the accelerating part of the (inspiratory or expiratory phases of) breathing cycle and the unsteady solution at the corresponding time instant of the decelerating part of the breathing cycle. Third, powerful and effective methods of pictorial representation are innovated, through which stunning visualizations of the accurately computed flow fields have been made possible.

II. MODEL OF THE HUMAN BRONCHIAL TREE

A three-dimensional model of the human bronchial tree is constructed by successively connecting cylindrical sections representing the airways of a particular generation with those of the next generation through bifurcation modules.¹ A particular generation in the network is referred here by the symbol G_n , where the index n denotes the generation number and progressively takes the integer values 0, 1, 2, etc. The six-generation network considered here consists of generations G_0 to G_5 (comprising 63 cylindrical sections and 31 bifurcation modules). The dimensions of the branches considered in this study are shown in Table I. The bifurcation angle (angle between two daughter branches emanating from the same mother branch) is set to 70° for all generations. All the branches are denoted by four characters “ $G_n B_k$,” where “ G_n ” denotes the generation to which the branch belongs, while “ B_k ” denotes the branch number in a particular generation. The cross-sectional plane at the start of the straight section of a branch (during inspiratory flow) is denoted by “ $G_n S_k$ ” (shown in Figs. 1 and 2), where “ k ” denotes the branch number in a particular generation. Similarly, the cross-sectional plane at the end of the straight section of a branch (during inspiratory flow) is denoted by “ $G_n P_k$.”

Figure 1 shows a three-dimensional view of the symmetric model of the human bronchial network with all the branches arranged in the in-plane configuration. For this arrangement of branches, the centrelines of all the cylindrical sections and the connecting bifurcation modules lie on a single plane (which is denoted by the term “meridional plane”).¹ In spite of the planar nature of this configuration, the complexity of the three-dimensional internal flow passages makes it necessary to perform three-dimensional computer simulations for determining the fluid flow field. The branches in a generation in the in-plane configuration are numbered from left to right as shown in Fig. 1. Since the branching network shown here is symmetric, only the branches lying in the left half (i.e., those originating from $G_1 B_1$) are shown in the figure. However, all

TABLE I. Dimensions for the first six generations of the human bronchial tree according to Weibel.³⁵

Generation number	Diameter d_{branch} (mm)	Length L (mm)
G_0 (trachea)	18.00	120.00
G_1	12.20	47.60
G_2	8.30	19.00
G_3	5.60	7.60
G_4	4.50	12.70
G_5	3.50	10.70

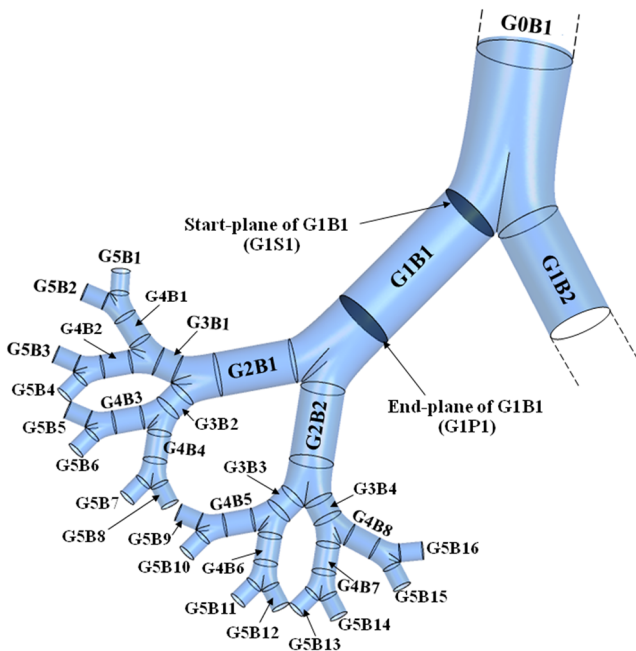


FIG. 1. Six generations (G0-G5) of a symmetric model of the human bronchial tree; in-plane configuration. (Only half of the network is shown here. Simulations are run for the entire network.)

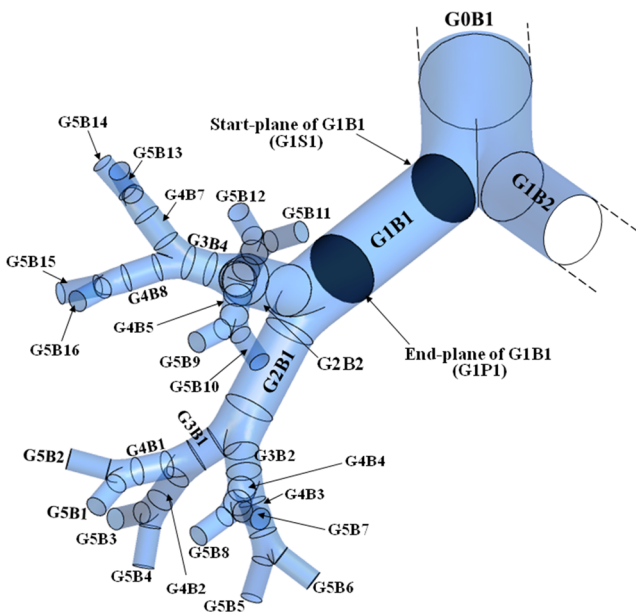


FIG. 2. Six generations (G0-G5) of a symmetric model of the human bronchial tree; out-of-plane configuration. (Only half of the network is shown here. Simulations are run for the entire network.)

simulations performed in the course of this study are run for the entire network.

A branching network comprising six generations of branches arranged in the out-of-plane configuration is shown in Fig. 2. Although the dimensions of the branches and the bifurcation angles for this network are the same as those in the in-plane configuration, the three-dimensional arrangement of the branches is different. For a comprehensible description of the complex three-dimensional arrangement consider the orientations of various overlapping units of the network, each unit comprising a bifurcation module, a preceding mother branch and two succeeding daughter branches—all of which must have centrelines lying on a single plane. For a particular unit U_n , suppose this plane is denoted by A_n . Now, consider a succeeding unit $U_{n+1,1}$ for which one of the daughter branches of unit U_n acts as the mother branch. Similarly, one can think of another unit $U_{n+1,2}$, considering the second daughter branch of U_n . Then, the planes in which $U_{n+1,1}$ and $U_{n+1,2}$ lie are at right angle to plane A_n , while maintaining the bifurcation angle between themselves. Since the complex three-dimensional arrangement of branches makes it difficult to describe how branches belonging to the same generation are numbered for the out-of-plane configuration, Fig. 2 provides a pictorial guide to the system followed for naming the branches.

III. SOLUTION METHODOLOGY

The present analysis considers the laminar three-dimensional flow of a viscous and incompressible fluid through a branching network comprising generations G0-G5 of a symmetrical model of the human bronchial tree. The three-dimensional model for the branching network is built in SolidWorks 2010,³⁶ and the meshing and numerical simulations are performed on the ANSYS Workbench³⁷ using the ANSYS Mesh Modeler and FLUENT, respectively. All computations are performed on a desktop computer with i5-3470 processor and 20 GB RAM.

A. Mathematical formulation

The present study pertains to laminar incompressible flow of a viscous fluid through six generations of a dichotomous branching network. The conservation equations for mass and momentum are given as follows:

$$\nabla \cdot \vec{v} = 0, \tag{1}$$

$$\rho \left[\frac{\partial \vec{v}}{\partial t} + (\vec{v} \cdot \nabla) \vec{v} \right] = -\nabla p + \mu \nabla^2 \vec{v}, \tag{2}$$

where \vec{v} represents the velocity vector of the fluid, ρ is the fluid density, p is the static pressure, and μ is the dynamic viscosity of the fluid. In the present set of simulations, ρ and μ are taken as 1.225 kg/m^3 and $1.7894 \times 10^{-5} \text{ kg/(m s)}$, respectively.

A time-varying but spatially uniform velocity is prescribed at the cross-sectional boundary of the first branch (G0B1) of the network. The temporal variation is represented by a sinusoidal function to model a breathing cycle,²⁹

$$V_{G0S1} = V_{\max} \sin(2\pi ft). \tag{3}$$

Here, V_{G0S1} is the axial velocity at the cross-sectional plane, V_{\max} is the maximum axial velocity at that cross section, f is the frequency of breathing (per second), and t is the time instant in the oscillatory flow. Considering resting conditions when the breathing frequency

is 12 per minute (time period T for one breathing cycle is 5 s), f is taken as $12/60 \text{ s}^{-1}$. Assuming a tidal volume of 500 ml, all of which is to be inhaled in the inspiratory phase ($0 \leq t \leq T/2$), the value of V_{\max} is set at 1.235 m/s. The branch walls are assumed to be rigid and smooth. Figure 3 gives a graphical representation of the temporal variation of the velocity prescribed at the boundary of the first generation. For the sinusoidal variation considered here, peak inspiration ($V_{G0S1} = V_{\max}$) occurs at $t = T/4$ while peak expiration ($V_{G0S1} = -V_{\max}$) occurs at $t = 3T/4$. The Reynolds number ($Re \equiv 2\rho V_{G0S1} R_{G0B1} / \mu$) in the first generation at maximum flow rate for $V_{\max} = 1.235 \text{ m/s}$ is calculated to be 1522.

It is to be noted that the spatially uniform velocity profile applies only at the start plane of generation G0; the solution of the Navier-Stokes equations produces spatial nonuniformity at all other cross sections of the network. Our computational experience shows that the prescription of the inlet velocity ensures, in incompressible flow, the correct volume (and mass) flow rate at all cross sections of the branch G0B1 (trachea) at any time-instant of the flow cycle but does not inhibit the development of a realistic nonuniform velocity profile in this branch even during the expiratory phase. Solutions presented later in Sec. IV D show the existence of nonuniform velocity distribution over most of the length of G0B1 during the expiratory phase. The length over which the transition from nonuniform to uniform flow occurs is very small, and this small length may be added before the start plane of G0B1 as a computational artifact.

Oscillatory flows are often described by the dimensionless parameter called the Womersley number defined as follows:¹⁸

$$\alpha = R \sqrt{\frac{2\pi f \rho}{\mu}}, \quad (4)$$

where R is the tube radius, f is the frequency of breathing (per second), and ρ and μ are the density and dynamic viscosity of the fluid. The Womersley number gives a measure of the ratio of

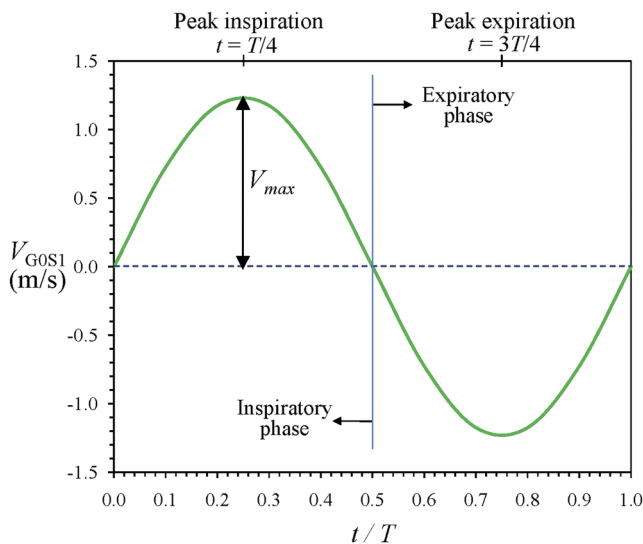


FIG. 3. Schematic representation of the oscillatory flow prescribed at the boundary (start plane) of the first branch G0B1 of the network.

unsteady effects to viscous effects.^{18,38} In other words, if the value of α is less than unity, the flow can be considered quasisteady because the low frequency lets the flow field develop fully during each cycle. If, on the other hand, the Womersley number is greater than unity, unsteady effects gain importance. In the present case, $f = 12/60 \text{ s}^{-1}$, $\rho = 1.225 \text{ kg/m}^3$, $\mu = 1.7894 \times 10^{-5} \text{ kg/(m s)}$, and $R_{G0B1} = 0.009 \text{ m}$; the Womersley number in generation G0 (α_{G0}) turns out to be 2.64.

B. Mesh generation

The branch diameter gradually decreases from 18 mm in the first generation to 3.5 mm in the last generation of the three-dimensional branching network comprising six generations (G0-G5). Therefore, a multiblock meshing scheme is adopted such that the relative size of the computational cells with respect to the branch dimensions remains approximately constant. ANSYS Meshing is used for generating an unstructured mesh in the three-dimensional network with sufficiently large number of tetrahedral elements.³⁹ The strong gradients near the solid walls are captured by applying boundary layer type meshing (inflation layers) there, with sufficiently small thickness of the first layer. The number of layers of the boundary layer type mesh is selected such that the height of the last layer is comparable to the size of the neighboring interior cell. The most critical portion of the geometry from a meshing point of view is the bifurcation module where complex cross-sectional changes take place as the single circular tube transforms into two separate circular tubes.¹ While previous studies implementing structured mesh⁴⁰ have usually not used any boundary layer type meshing, others using unstructured meshes³⁸ along with boundary layer type meshing suffer from intersection of the inflation layers in the bifurcation modules. This intersection is due to the fact that the bifurcation module is usually constructed by combining two separate but overlapping narrowing tubes (each connecting the mother branch to one of the daughter branches) and the inflation layers are separately applied to the two narrowing tubes. In the present work, while constructing the geometry in SolidWorks,³⁶ the bifurcation modules are created as a single geometric part connecting the mother and daughters. This ensures that the inflation layers closely follow the shape of the walls of the bifurcating module without intersecting with one another.

C. Numerical method

The governing equations [Eqs. (1) and (2)] are solved numerically with the help of the commercial computational fluid dynamics (CFD) package FLUENT that uses a finite volume technique. The available pressure-based solver is used here. The diffusion terms are discretized using a central difference scheme. A second order upwind scheme is used to discretize the advection terms in the unstructured three-dimensional mesh, so as to reduce the numerical diffusion.⁴¹ An implicit,⁴² second-order temporal discretization was employed for the unsteady simulations. A segregated solver is used to solve the resulting system of equations. The SIMPLE algorithm is used to couple the velocity and pressure for solving the governing equations. The default values³⁷ of the under-relaxation factors in Fluent are used for the simulations. At each time step, iterations are performed till the scaled residuals³⁷ for continuity and momentum equations reach 10^{-8} .

The time-varying sinusoidal velocity [Eq. (3)] at the boundary of the first generation of the branching network is specified with the help of a user-defined function in FLUENT. The no-slip and no-penetration conditions are applied on the walls of the branches using the “Wall” boundary condition in FLUENT. Since there is a dearth of knowledge regarding the pressure conditions at the end of the generation G5 in the human bronchial tree, previous researchers^{43–45} have resorted to a pressure condition at the end of the branches of the last generation considered. Taking cue from such studies, a pressure boundary condition has been used in the present study using the “Pressure Outlet” boundary condition feature of FLUENT. This feature requires the specification of the gauge static pressure at the outlet boundary, which is then used as a reference to calculate the pressure throughout the computational domain. The gauge static pressure at the outlets is set to zero in the present set of simulations. The CFD simulations determine the change in static pressure between the inlet and outlet of the network (Δp_{io}). It is assumed that, for incompressible flow, Δp_{io} does not vary with the absolute value of static pressure specified at the outlet. Thus, once the pressure difference between the inlet and any location in the network is determined from the CFD simulation, the absolute value of static pressure at that location can be calculated from the known value of static pressure at the inlet.

In addition to the unsteady simulation covering the entire breathing cycle, separate steady state solutions are run at each selected time instant (with the same boundary condition at G0S1 at the same time instant as is employed in the unsteady simulation) in order to determine by what extent the unsteady solutions differ from their steady flow counterparts. The solver³⁷ uses a time-marching technique^{46,47} to obtain a steady-state solution as the limiting process of an unsteady simulation.

The velocity at a point in the flow domain may be resolved into two mutually perpendicular components: one along the normal to the relevant cross-sectional plane (primary velocity \vec{v}_p) and the other along the cross-sectional plane (secondary velocity \vec{v}_s). The algorithm used for the determination of the primary and secondary velocity components is given in Ref. 2.

D. Grid and time step independence study

A comprehensive grid independence study has been performed for the G0-G5 networks following the methodology suggested by Roache.⁴⁸ Here, the flow in the G0-G5 network is simulated using four meshes: “coarse,” “medium,” “fine,” and “very fine.” For the in-plane configuration, the “coarse,” “medium,” “fine,” and “very fine” meshes, respectively, contain approximately 1020×10^3 , 4173×10^3 , $14\,084 \times 10^3$, and $30\,942 \times 10^3$ computational elements (finite volume cells). For the out-of-plane configuration, the “coarse,” “medium,” “fine,” and “very fine” meshes, respectively, contain 1028×10^3 , 4211×10^3 , $14\,214 \times 10^3$, and $31\,229 \times 10^3$ computational elements. A grid convergence index (*GCI*) was defined for the refined mesh by the following expression:⁴⁸

$$GCI_{fine} = F_s \frac{\epsilon_{rms}}{r_{grid}^q - 1}. \quad (5)$$

Here, q (=2 in the present study) is the order of discretization of all terms in space, F_s is the factor of safety, and r_{grid} is the grid refinement factor defined as $r_{grid} = (N_{fine}/N_{coarse})^{1/3}$, where N is the

number of elements in the mesh. ϵ_{rms} is the root-mean-square value of the relative error [$\epsilon = (\phi_{i,coarse} - \phi_{i,fine})/\phi_{i,fine}$] calculated over a sufficiently large number of points. Usually, a value of ϵ_{rms} around 2% is assumed to indicate a high quality grid-converged solution.³⁹ For $r_{grid} = 1.5$, $q = 2$, and $F_s = 3$, the value of *GCI* corresponding to $\epsilon_{rms} = 0.01$ can be calculated to be 2.4%. In the course of our present series of studies^{1,2} on the topic, we found that for $GCI \leq 5\%$, the flow field changes negligibly with further grid refinements.

Celik *et al.*⁴⁹ proposed a formulation for calculating an apparent order of discretization from values of ϵ_{rms} and r_{grid} . They stated that an agreement of the apparent order with the formal order of the used scheme can be taken as a good indication of the grids being in the asymptotic range. Accordingly, here we have used the two values each of ϵ_{rms} and r_{grid} , for the two sets of three meshes (coarse, medium, and fine; and medium, fine, and very fine), to iteratively find a value of q .⁴⁹ The closer the value of q comes to its original value (i.e., $q = 2$ for the adopted second-order spatial discretization), the better the grid independence.

We find that for the in-plane configuration, the value of *GCI* for the medium mesh is 9.82%, that for the fine mesh is 2.58%, and that for the very fine mesh is 1.76%. Hence, the change in *GCI* between fine and very fine mesh is small. The value of q is calculated⁴⁹ to be 1.92 for the two sets of three meshes (coarse, medium, and fine; and medium, fine, and very fine). Similarly, for the out-of-plane configuration, we find that the value of *GCI* for the medium mesh is 11.68%, that for the fine mesh is 3.30%, and that for the very fine mesh is 2.18%. Hence, the change in *GCI* between fine and very fine mesh is small. The value of q is calculated to be 2.05 for the two sets of three meshes (coarse, medium, and fine; and medium, fine, and very fine). Hence, for both configurations, the “fine” mesh (containing about 14×10^6 computational elements) is used for subsequent simulations.

A systematic study has also been performed to ensure that the solutions reported in the paper are independent of the size of the time step. For this purpose, we have run simulations using the “fine” mesh for both configurations using three values of the time step size Δt , viz., $\Delta t = 0.025$ s, $\Delta t = 0.01$ s, and $\Delta t = 0.005$ s. It is found that the velocity magnitudes along a diameter on the end plane of G1B1 obtained by using $\Delta t = 0.025$ s and $\Delta t = 0.01$ s show a maximum difference of about 5%, while that obtained by using $\Delta t = 0.01$ s and $\Delta t = 0.005$ s show a maximum difference of less than 1%. Similar findings are made for the solutions at other locations of the network. Based on such calculations, we have used $\Delta t = 0.01$ s for all subsequent simulations reported here.

All simulations are performed on a desktop computer with i5-3470 processor and 20 GB RAM, using the parallel processing feature of FLUENT (four processors are utilized here). The use of double-precision arithmetic and small value of the convergence criteria (10^{-8}) ensures the accuracy of the solution at all instants of the oscillatory cycle, especially at those instants when the net mass flow rates in the network are small. The time taken to achieve spatially converged solution, for the “fine” mesh containing 14×10^6 elements, at each time step is approximately 1 h. For an oscillatory cycle of time period $T = 5$ s, and a time step size of $\Delta t = 0.01$ s, calculations need to be performed for 500 time steps. The time taken to obtain a converged solution for the complete cycle is about 500 h. Since we have simulated two cycles to ensure that start-up effects are absent, the total time taken to obtain the results reported here is

about 1000 h. Three such complete simulations are reported in the present work (in-plane at $\alpha = 2.64$, out-of-plane at $\alpha = 2.64$, in-plane at $\alpha = 10$, thus totaling 3000 h of computation time). The task is therefore computationally challenging and time-consuming. Spatial and temporal accuracy of the solution is demonstrated in Sec. III E so that dependable physical conclusions can be made from the simulations presented.

E. Validation of results

The present numerical method was validated through comparisons with the experiments of Lieber and Zhao²⁶ on oscillatory flow in a bifurcation. The geometry of Zhao and Lieber¹⁷ is reproduced here, and the velocity profile is compared along the diameter lying on the meridional plane at the outlet of the left daughter branch (Fig. 4). At $t = 2T/10$, flow is in the inspiration phase and the velocity profile in the meridional plane is skewed toward the inner edge of the bifurcation because of the flow path curvature. At $t = 7T/10$, flow is in the expiration phase and the diametrical velocity profile is nearly parabolic with a maximum velocity at the center of the cross-section. It is found that the present CFD results agree well with the experimental measurements.²⁶ A comparison of the CFD results obtained by using the same numerical methodology with experimental data³ for the steady flow through a bifurcation may be found in Ref. 1.

The critical Reynolds number in a branching network is likely to be lower than that in a straight pipe^{50,14} though we have been unable to find any systematic study of instability in a bifurcating network or any definitive value of the relevant critical Reynolds number in the literature. The excellent matching of the computed results at various time instants of the cycle having a maximum Reynolds number of 2077 with the experimental data gives confidence on the dependability of the present computations and suggests that the laminar assumption works well up to such Reynolds number which is comfortably greater than the maximum value $Re_{G0S1} = 1522$, at the peak inspirational flow rate, used for the reported computations in the rest of the paper.

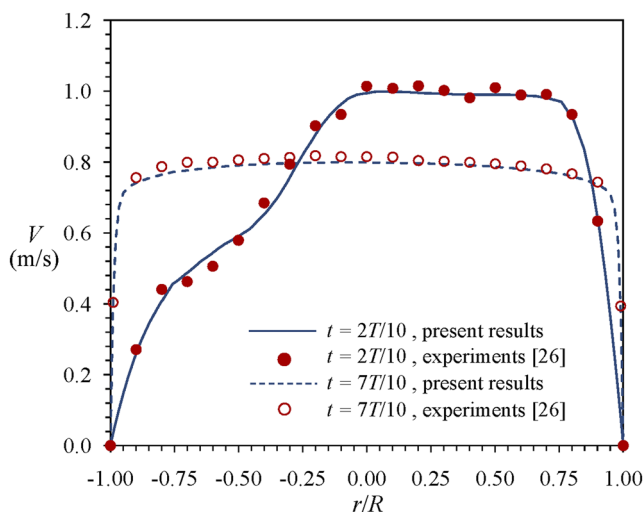


FIG. 4. Comparison of the present CFD results with previous experiments on oscillatory flow in a bifurcation at $Re_{max} = 2077$.

IV. RESULTS AND DISCUSSION

In the present work, we have simulated the oscillatory flow in a six-generation (G0-G5) branching network, the adopted geometry being a generalized model of the human bronchial tree. A breathing frequency of 12 breaths per minute has been assumed which corresponds to the resting condition in a normal human adult. Two breathing cycles (each of 5 s duration) were simulated, of which results for the second cycle are reported below so that any small start-up effect is avoided. All computations given in Secs. IV A–IV D are performed at $\alpha_{G0} = 2.64$.

A. Spatial evolution of the velocity field during a breathing cycle

Results are presented here at four instants in the breathing cycle, viz., peak inspiration ($t = T/4$), end of inspiration/beginning of expiration ($t = T/2$), peak expiration ($t = 3T/4$), and end of expiration/beginning of inspiration ($t = T$ or $t = 0$). Here, the primary velocity is taken positive for flow in the direction G0-G5 (inspiratory flow), while it is taken negative when flow occurs from G5 to G0 (expiratory flow). The representational convention is such that, in all the diagrams of flow cross sections given in Secs. IV A 1 and IV A 2, positive value of primary velocity indicates that the flow is toward the reader and the downstream bifurcation ridge would appear as a vertical line on the plane of cross sections.

1. Results for the in-plane configuration

Figure 5 shows the flow field at the end planes of the branches of generations G0-G3 at $t = T/4$ (peak inspiration). The vectors of the secondary velocity are superposed on the contours of primary velocity at the selected cross-sectional planes. The instantaneous value of the Reynolds number at $t = T/4$ is found to be 1522. The primary velocity contour at plane G0P1 is characterized by concentric circles with the maximum velocity at the center of the cross section (similar to the flow in a pipe). The secondary velocity at G0P1 shows inward motion of fluid from the periphery toward the center, which may be attributed to the change of cross-sectional shape as the first bifurcation module is approached.² The primary velocity at plane G1P1 is characterized by a skewed distribution with the maximum velocity shifted toward the inner edge of the preceding bifurcation. Since the fluid traverses only one bifurcation along its path from the inlet to plane G1P1, Dean-type secondary motion² is observed here with the fluid being pushed toward the inner edge of the preceding bifurcation along the horizontal diameter and back toward the outer edge of that bifurcation along the top and bottom edges.

The contours of primary velocity at planes G2P1 and G2P2 at $t = T/4$ (peak inspiration) show a skewed distribution with maximum velocity shifted toward the inner edge of the preceding bifurcation. Moreover, owing to the asymmetry in the velocity distribution at plane G1P1 about the downstream bifurcation ridge, the maximum (and average) velocity at plane G2P2 is significantly greater than that at G2P1. The secondary velocity field at the end planes of the G2 branches is characterized by two pairs of vortices² as compared to the single pair found at G1P1. The primary velocity distribution at the end planes of all the G3 branches appear skewed toward the inner edge of the preceding bifurcation with the average velocity being greatest in branch G3B3. The secondary flow

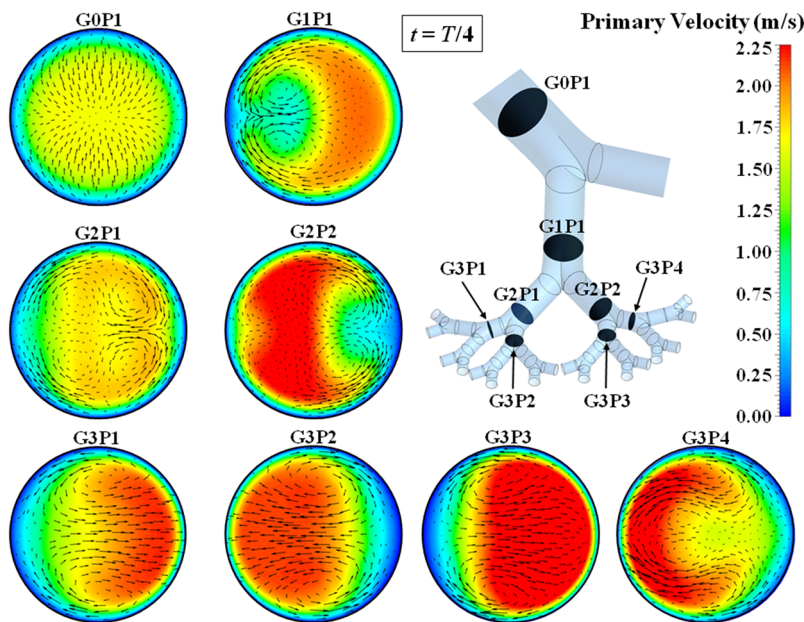


FIG. 5. Distribution of primary and secondary velocities at the specified planes in branches of generations G0-G3 at peak inspiration for in-plane configuration. (Vectors indicate secondary velocity, while the contours show magnitude of primary velocity.)

patterns in the G3 branches are characterized by typical Dean-type circulation (with two counter-rotating vortices).

In the Weibel model of human bronchial network as shown in Table I, the branch diameters for various generations are such that the total cross-sectional area of a generation decreases from G0 to G3 but increases from G3 onward, the area at G4 being equal to that at G0. The average velocity at a generation, therefore, increases from G0 to G3, which is borne out of the distributions shown in Fig. 5.

The contours of primary velocity at the end planes of the branches of generations G0-G3 at $t = T/2$ (end of inspiration/beginning of expiration) are shown in Fig. 6. As mentioned previously, negative values of the primary velocity indicate expiratory flow (i.e., in the direction G5-G0). Thus, Fig. 6 shows that at $t = T/2$, the flow in the branches of generations G0-G3 comprise both inspiratory and expiratory flows. The magnitude of the primary velocity at this instant of the breathing cycle is small throughout the network, but the inspiratory and expiratory flow velocities are of the

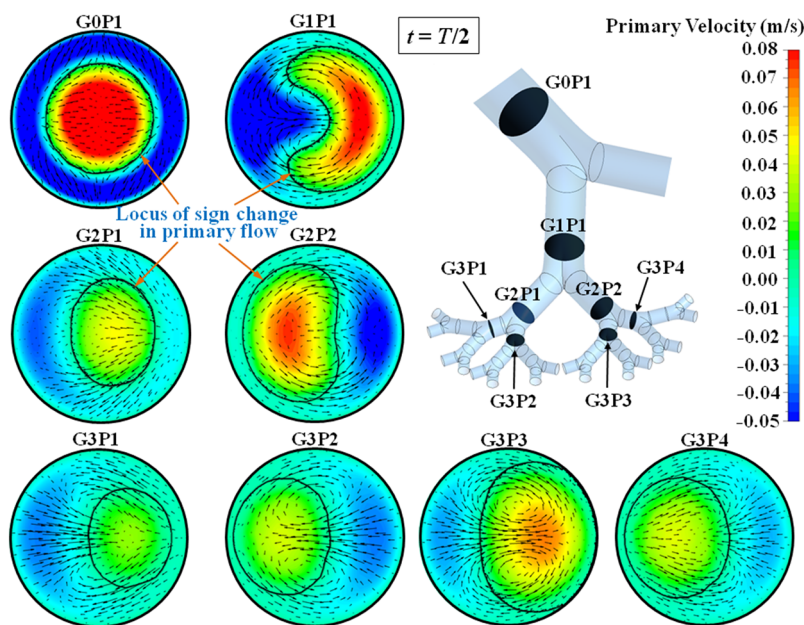


FIG. 6. Distribution of primary and secondary velocities at the specified planes in branches of generations G0-G3 at the end of inspiration for in-plane configuration. (Vectors indicate secondary velocity, while the contours show magnitude of primary velocity. The closed curves are painstakingly constructed through postprocessing to clearly demarcate two regions with opposite directions of primary velocity.)

same order of magnitude. The locus of change of sign of the primary velocity, which demarcates the inspiratory flow region from the expiratory flow region, has been indicated in each diagram. The reversal of flow direction from inspiratory to expiratory occurs near the walls where the prevailing inspiratory velocities at earlier instants were small due to viscous effects. The secondary flow patterns at most of the planes shown in Fig. 6 are characterized by Dean-type circulation with two counter-rotating vortices in each half of the cross section.²

It is to be appreciated that the prescribed volume flow rate at the computational boundary at $t = T/2$ is zero; thus, a steady flow solution would give zero velocity at every point of the computational domain. The nonuniform flow structure seen in Fig. 6 is thus entirely due to the unsteady effects. A striking feature of Fig. 6 is that (unlike how the average and maximum velocities vary down the generations from G0 to G5 at peak inspiration $t = T/4$) the range of velocity magnitude (negative to positive) at $t = T/2$ is the greatest in G0 and its value is progressively lower in G1, G2, G3, and so on. This apparently paradoxical variation can be explained in the following manner. The diameters of the branches progressively reduce down the generations from G0 to G5, and therefore, according to Eq. (4), the relevant Womersley number is the greatest in G0 and progressively reduces down the generations. Since the flow velocities at $t = T/2$ arise solely due to unsteady effects, the range of velocity (i.e., amplitude) displays the above-mentioned variation in different generations of a branching network.

Figure 7 shows the flow field at $t = 3T/4$ (peak expiration). A comparison of Figs. 5 and 7 show two important differences between the flow structures at peak inspiration and that at peak expiration. First, peak expiration (Fig. 7) is characterized by more symmetric velocity distributions (symmetry about both vertical and horizontal diameters in the diagrams), as compared to the significant asymmetry found in the cross-sectional distribution of the primary

velocity at the end planes of the branches of generations G1–G3 at peak inspiration. Second, during peak expiration, small regions of oppositely directed flow (i.e., inspiratory flow) are seen to occur near the walls in generations G0–G2. (No bidirectional flow is observed at this time instant in generations G3, G4, or G5. There is no bidirectional flow at peak expiration in the pipe solution of Womersley.¹⁸) However, the magnitudes of the positive velocities in these regions are an order of magnitude smaller than the expiratory flow velocities at the same cross section. The secondary flow at all the cross sections shown here (except G1P1) show four vortices in the four quarters of the cross section. At plane G1P1, eight vortices are found; four occurring at locations similar to that in the other planes and four occurring near the center of the cross section. While the occurrence of four vortices during expiratory flow has been reported previously,²⁶ the occurrence of eight vortices at G1P1 is reported here for the first time. The magnitude of prescribed volume flow rate at the computational boundary is the same at $t = T/4$ and $t = 3T/4$. The stunning visual difference between the flow structures in Figs. 5 and 7 thus displays the fundamental difference between the fluid dynamics of successively bifurcating flow and that of successively combinatory flow.

Figure 8 shows the flow field at $t = T$ (end of expiration/beginning of inspiration). As explained previously, the nonuniform flow structure seen in Fig. 8 is entirely due to the unsteady effects since a steady flow solution with the same boundary condition would have resulted in zero velocity everywhere in the flow field. As in Fig. 6 ($t = T/2$), the flow in the branches of generations G0–G3 at $t = T$ (Fig. 8) comprise both inspiratory and expiratory flows. Although the magnitude of the primary velocity at this instant of the breathing cycle is small throughout the network, the inspiratory and expiratory flow velocities are of the same order of magnitude. The locus of change of sign of the primary velocity, which demarcates the inspiratory flow from the expiratory flow, has been indicated in

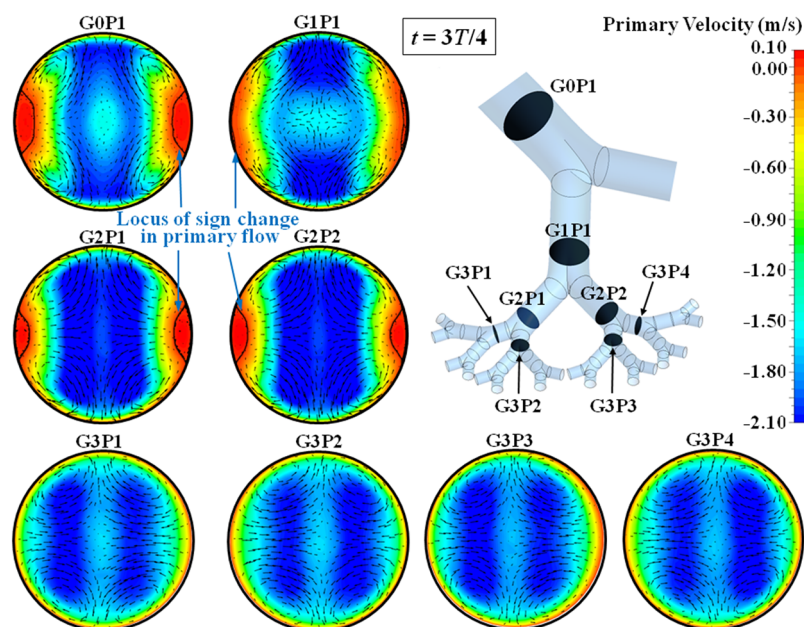


FIG. 7. Distribution of primary and secondary velocities at the specified planes in branches of generations G0–G3 at peak expiration for in-plane configuration. (Vectors indicate secondary velocity while the contours show magnitude of primary velocity. The closed curves are painstakingly constructed through postprocessing to clearly demarcate two regions with opposite directions of primary velocity.)

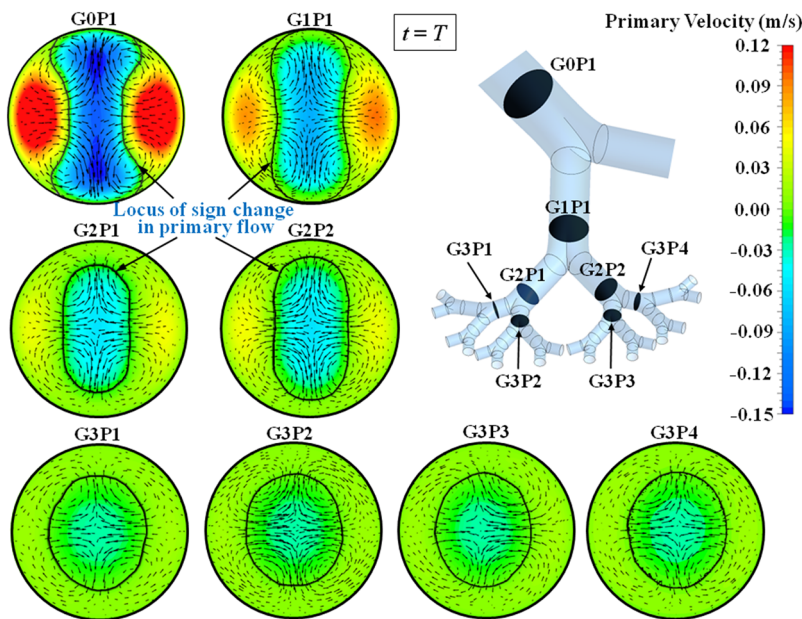


FIG. 8. Distribution of primary and secondary velocities at the specified planes in branches of generations G0-G3 at the end of expiration for in-plane configuration. (Vectors indicate secondary velocity while the contours show magnitude of primary velocity. The closed curves are painstakingly constructed through postprocessing to clearly demarcate two regions with opposite directions of primary velocity.)

each diagram. The range of velocity magnitude (negative to positive) at $t = T$ is the greatest in G0 and its value is progressively lower in G1, G2, G3 and so on. As explained in connection with Fig. 6, this reduction in range in velocity (i.e., amplitude) is caused by a reduction in the Womersley number down the generations.

Although the prescribed volume flow rate at the computational boundary is zero both at $t = T/2$ and at $t = T$, there are important differences between the unsteady flow solutions at these two instants. First, the distribution of the primary velocity over the cross section is quite different at the two time instants. Second, a comparison of Figs. 6 and 8 shows that while inspiratory flow occurred in the central regions (which are shifted toward the inner edge of the preceding bifurcation modules) with expiratory flow in the peripheral regions at $t = T/2$, the inspiratory flow is restricted to the peripheral regions while the expiratory flow occupies central regions (around the axis of the branch) at $t = T$. Third, the patterns of secondary flow at all the cross-sectional planes at $t = T$ shown in Fig. 8 are characterized by four vortices, while that at $t = T/2$ (shown in Fig. 6) were generally characterized by two vortices. It is thus established that the secondary flow patterns at $t = T/2$ and $t = T$ are related to the secondary flow structure occurring in the respective preceding part of the cycle. Thus, the secondary flow patterns at the end of inspiration (Fig. 6) appear similar to that observed at peak inspiration (Fig. 5), while the secondary flow at the end of expiration (Fig. 8) are qualitatively similar to that found during peak expiration (Fig. 7).

The positions of the vortices can be determined by visual inspection of the secondary flow patterns at a cross section shown in Figs. 5–8. In addition to this method, a second quantitative method, using the λ_2 criterion,⁵¹ is used to confirm the number and locations of the vortices. According to the λ_2 criterion, any point in the flow field, for which $\lambda_2 < 0$, is part of a vortex. Here, λ_2 is the median eigenvalue of the tensor $S^2 + \Omega^2$, where S is the symmetric part and Ω is the antisymmetric part of the velocity gradient tensor. The

method and its outcome in describing vortical structures in bifurcating networks are described in Ref. 2. The method is used here for the purpose of double-checking, but the outcome is not included in Figs. 5–8 to keep them less cluttered.

Although the branching network considered in the present study comprises generations G0 to G5, Figs. 5–8 show the cross-sectional velocity distribution in the branches up to generation G3 only. While the method of representation in the above-mentioned figures allows the simultaneous discussion of the primary and secondary flow patterns, it is difficult to include results for generations G4 and G5 (which would require the inclusion of 24 more cross-sectional diagrams: 8 for G4 branches and 16 for G5 branches). Hence, we have included the three-dimensional vector plots of velocity at the end planes of branches of generations G0 to G5 in the following four figures which provide complementary information regarding the flow structure. The colors of the vectors represent the magnitude of velocity, while the direction is borne by the orientation of the vectors themselves. It is to be noted that the lengths of the vectors do not signify the actual velocity magnitude but are suitably adjusted to avoid overlapping in the diagram.

Figure 9 shows the velocity vector plots at the end planes of branches of generations G0-G5 at $t = T/4$ (peak inspiration). At this instant, the flow is entirely inspiratory throughout the network with no flow reversal (expiratory flow) in any branch. As discussed in the context of Fig. 5, the velocity distributions at all the planes in Fig. 9 show a skewed nature with the maximum velocity shifted toward the inner edge of the preceding bifurcation module. The velocity distributions at most of the cross-sectional planes shown in Fig. 9 show a single peak. It is also found that the average (and maximum) velocity is greatest along the path G0B1-G1B1-G2B2-G3B3-G4B6-G5B11 for the G0-G5 network considered in the present work. On the other hand, the average (and maximum) velocity is the smallest along the path G0B1-G1B1-G2B1-G3B1-G4B1-G5B1. Along the maximum

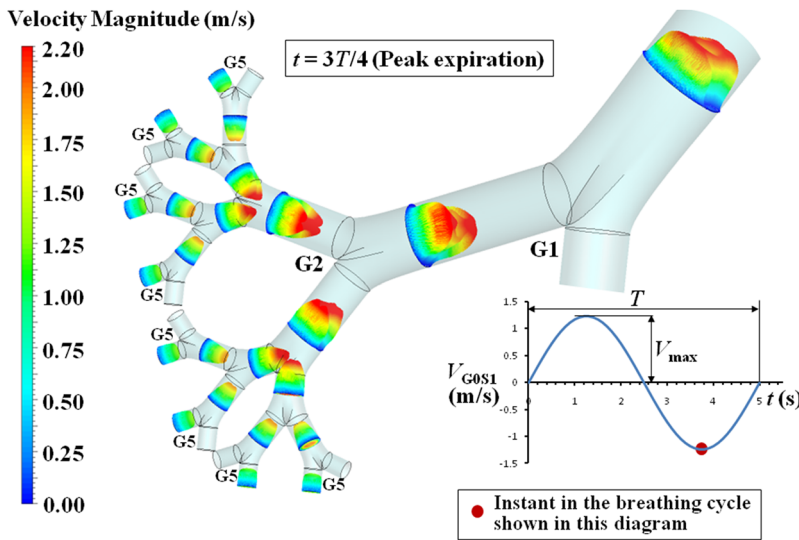


FIG. 11. The vectors of velocity at selected cross-sectional planes showing the three-dimensional evolution of the flow field at peak expiration; in-plane configuration.

inspiration. This may be attributed to the changed geometry of the flow path during inspiration and expiration. During inspiration, as the flow traverses a bifurcation module joining a mother branch (generation G_n) to its two daughter branches (generation G_{n+1}), the curvature in the flow path is such that the maximum cross-sectional velocity is shifted toward the inner edge of the bifurcation module in both daughter branches. This skewed velocity distribution in the daughter branches leads to asymmetric mass-flow distribution among the downstream branches of the daughters. On the other hand, during expiration, as the flow traverses a bifurcation module joining two branches of generation G_{n+1} to a branch of generation G_n , the curvature of the flow path pushes the maximum velocity toward the center of the cross section in the G_n branch. This results in more symmetric velocity distribution in the G_n branch leading to a reduction in the asymmetry in the mass flow distribution among

the downstream (G_{n-1}) branches. An interesting observation that may be made in Fig. 11 is that the velocity distributions at most of the planes show four central peaks (which merge along the straight length of a branch to give a plateaulike distribution) as compared to the single peak occurring during the inspiratory phase. This may again be attributed to the joining of the two fluid streams at each bifurcation module during expiration as opposed to the division into two streams during inspiration.

Figure 12 shows the velocity vectors on specified planes at $t = T$ (end of expiration/beginning of inspiration). The magnitudes of velocity at this instant of the breathing cycle are significantly smaller than that at peak expiration. As discussed in the context of Fig. 8, both inspiratory and expiratory flows exist at this instant of the breathing cycle. The velocity field at all the cross-sectional planes shown in Fig. 12 are characterized by a region of

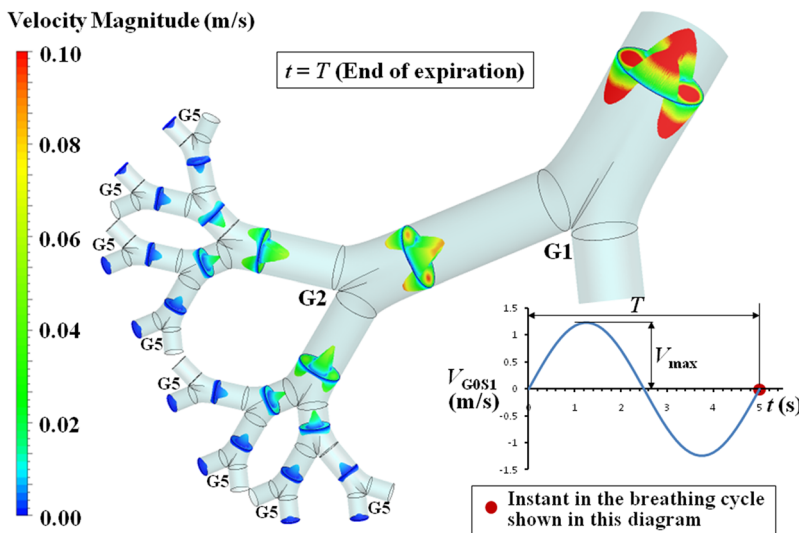


FIG. 12. The vectors of velocity at selected cross-sectional planes showing the three-dimensional evolution of the flow field at the end of expiration; in-plane configuration.

expiratory flow which is located near the center of the cross section, and inspiratory flow surrounding the expiratory flow region. Since this figure corresponds to end of expiration/beginning of inspiration ($t = T$), the expiratory flow prevails in those regions where the velocity magnitude was significant during the expiratory phase, while inspiratory flow develops in regions where the velocity was small during expiration. Thus, the simultaneous existence of inspiratory and expiratory flow may be attributed to flow inertial effects.

A comparison of Figs. 10 and 12 show that bidirectional flow exists at both time instants $t = T/2$ and $t = T$, but there are differences in the details of the velocity distribution. At $t = T/2$, one inspiratory peak and one expiratory peak are observed at a cross section. At $t = T$, two expiratory peaks and two inspiratory peaks are observed. This difference is the manifestation of different degrees of cross-sectional flow asymmetry developed in the respective preceding part of the cycle.

2. Results for the out-of-plane configuration

In this section, we present the evolution of the velocity field in the out-of-plane configuration of the branching network. The velocity contours and vectors are located at similar locations in the branching network as was presented in Sec. IV A 1 to make comparisons easier. The adopted representational convention is also similar to that used in Sec. IV A 1; the positive primary velocity indicates that the flow is toward the reader and the downstream bifurcation ridge would appear as a vertical line in the diagram.

Figure 13 shows the flow field at the end planes of the branches of generations G0-G3 at peak inspiration ($t = T/4$). The vectors of secondary velocity are superposed on the contours of primary velocity at the selected cross-sectional planes. The instantaneous value of the Reynolds number at $t = T/4$ is 1522. The primary velocity

contours as well as the secondary flow pattern at plane G0P1 are identical with those found for in-plane configuration (Fig. 5). The flow structures at G1P1 are also qualitatively same as was found in Fig. 5 but appear rotated through 90° due to the adopted representational convention. While the velocity contours at planes G2P1 and G2P2 were found to be different from one another (Fig. 5) for the in-plane configuration, it is found in Fig. 13 that the same are mirror images of one another for the out-of-plane configuration. This is due to the fact that the 90° rotation of successive flow units¹ in the out-of-plane configuration leads to symmetry of the velocity distribution at G1P1 and G1P2 about their downstream bifurcation ridges; as a consequence, the flow structures at G2P1 and G2P3 are identical, those at G2P2 and G2P4 are identical, while the flow structures at G2P1 and G2P2 (and those at G2P3 and G2P4) are mirror images to one another. However, unlike what happens for in-plane counterparts, the velocity fields at any of the four planes (G2P1, G2P2, G2P3, G2P4) in out-of-plane configuration do not possess any line of symmetry, thus indicating that the velocity fields in all of their respective downstream branches are different from one another. Hence, the primary velocity contours at planes G3P1 and G3P2 in Fig. 13 are not only different from one another but also possess no line of symmetry in the cross section. The velocity contours at G2P1 and G2P2 being mirror images to one another, the velocity contours at G3P1 and G3P4, and those at G3P2 and G3P3 are, respectively, mirror images of one another.

While the secondary flow pattern at the end planes of the G2 branches were characterized by two pairs of vortices² for the in-plane configuration (Fig. 5), it is observed in Fig. 13 that plane G2P1 (and G2P2) shows the presence of three vortices. The secondary flow at the end planes of the G3 branches again show the existence of two vortices. These observations are in-line with those reported in Ref. 2 for steady inspiratory flow in the same branching network. As in the case of Figs. 5-8, the positions of the vortices in Figs. 13-16 are

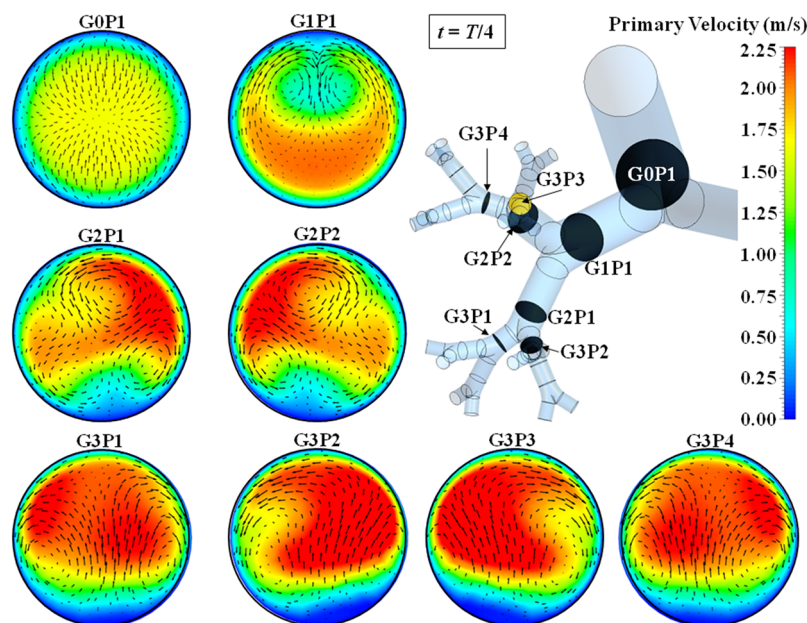


FIG. 13. Distribution of primary and secondary velocities at the specified planes in branches of generations G0-G3 at peak inspiration for out-of-plane configuration. (Vectors indicate secondary velocity while the contours show magnitude of primary velocity.)

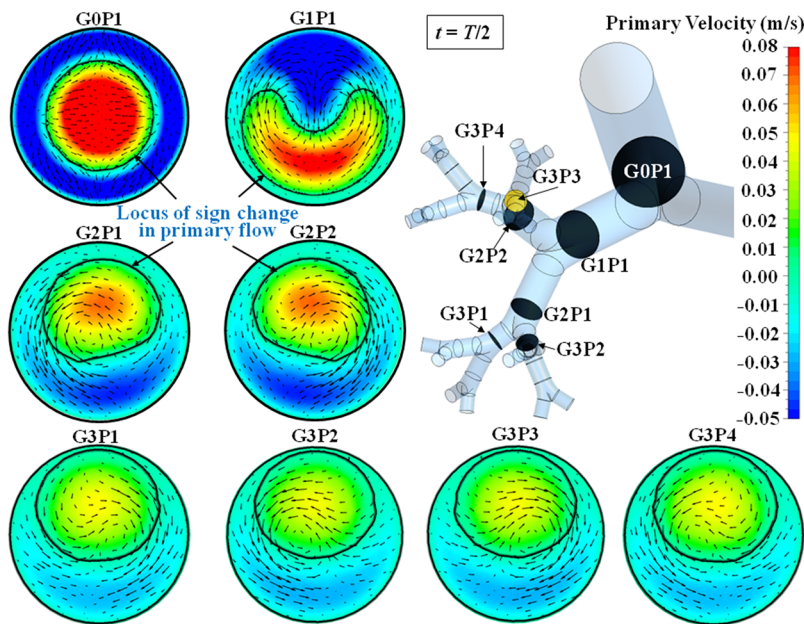


FIG. 14. Distribution of primary and secondary velocities at the specified planes in branches of generations G0-G3 at the end of inspiration for out-of-plane configuration. (Vectors indicate secondary velocity while the contours show magnitude of primary velocity. The closed curves are painstakingly constructed through postprocessing to clearly demarcate two regions with opposite directions of primary velocity.)

confirmed by using the λ_2 criterion in addition to a visual inspection of the secondary flow patterns at the cross section.

Figure 14 shows the velocity fields at the end planes of the branches of generations G0-G3 at $t = T/2$ (end of inspiration/beginning of expiration). As mentioned previously, negative values of the primary velocity indicate expiratory flow. Thus, Fig. 14 shows that at $t = T/2$, the flow in the branches of generations G0-G3 comprise both inspiratory and expiratory flows. It is to be appreciated that the prescribed volume flow rate at the

computational boundary at this time instant of the cycle is zero and thus the nonuniform flow structures seen in Fig. 14 are entirely due to the unsteady effects. While the magnitude of the primary velocity at this instant of the breathing cycle is small throughout the network, the inspiratory and expiratory flow velocities are of the same order. The locus of change of sign of the primary velocity, which demarcates the inspiratory flow from the expiratory flow, has been indicated in each plot. The range of velocity magnitude (negative to positive) at $t = T/2$ is the greatest in G0 and its value is progressively

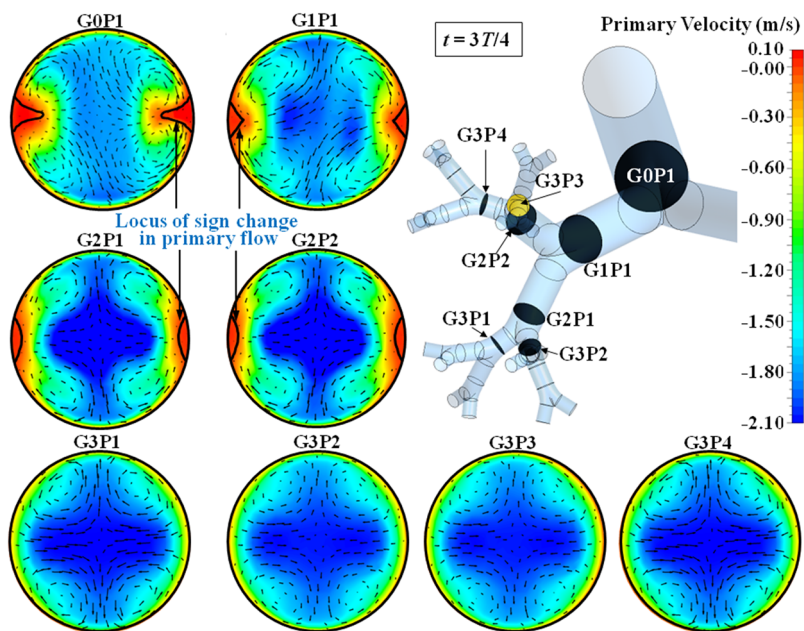


FIG. 15. Distribution of primary and secondary velocities at the specified planes in branches of generations G0-G3 at peak expiration for out-of-plane configuration. (Vectors indicate secondary velocity while the contours show magnitude of primary velocity. The closed curves are painstakingly constructed through postprocessing to clearly demarcate two regions with opposite directions of primary velocity.)

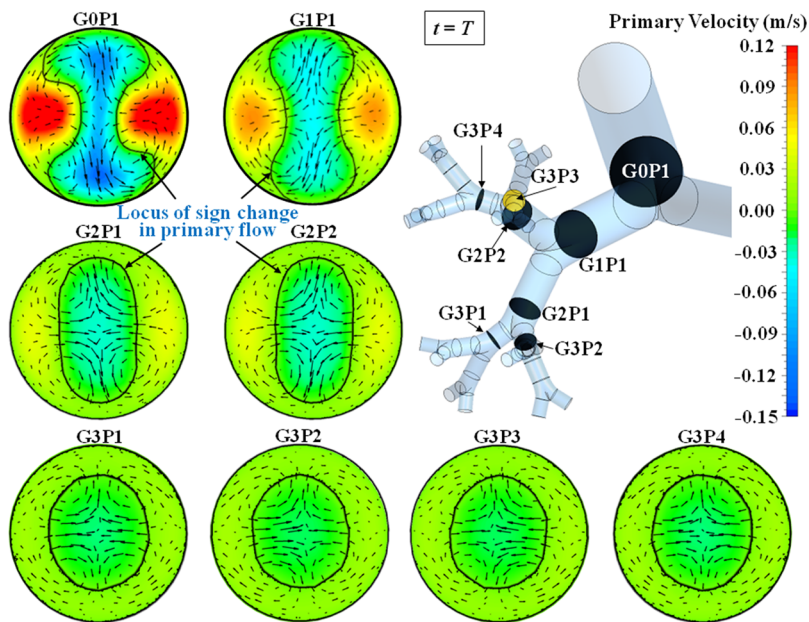


FIG. 16. Distribution of primary and secondary velocities at the specified planes in branches of generations G0-G3 at the end of expiration for out-of-plane configuration. (Vectors indicate secondary velocity while the contours show magnitude of primary velocity. The closed curves are painstakingly constructed through postprocessing to clearly demarcate two regions with opposite directions of primary velocity.)

lower in G1, G2, G3, and so on. As explained in connection with Fig. 6, this reduction in range in velocity (i.e., amplitude) is caused by a reduction in the Womersley number down the generations.

A comparison of Figs. 6 and 14 shows that the flow field is almost identical for the in-plane and out-of-plane configurations up to the end plane of branches of generation G1. Positive velocities (i.e., inspiratory flow) are observed in those regions of the cross section where the primary velocity was high during inspiration. On the other hand, those regions in the cross sections which showed low velocities during inspiration are characterized by negative velocities at the time instant $t = T/2$ (i.e., at the end of inspiration). Thus, the reversal of flow direction from inspiratory to expiratory may be attributed to the effects of flow inertia. Although the velocity contours at the end planes of the G2 and G3 branches for the out-of-plane configuration are significantly different from those for the in-plane arrangement of branches, the same generic trend of positive velocities in regions where the velocity was high during inspiration holds true there as well.

The secondary flow patterns at planes G1P1 in Fig. 14 are characterized by Dean-type circulation.⁴ However, the secondary flow in branches of generations G2 and G3 show a single vortex in the cross section. This is in contrast to the existence of a pair of vortices at all these locations for the in-plane configuration (Fig. 6). It is interesting to note that, for the out-of-plane configuration, the three- and two-vortex systems in the G2 and G3 branches, respectively, at peak inspiration ($t = T/4$) are replaced by the relatively less complex single vortex system at the end of inspiration ($t = T/2$). This may be attributed to the significantly smaller velocities at $t = T/2$ as compared to that at $t = T/4$ (peak inspiration).

Figure 15 shows the velocity fields at $t = 3T/4$ (peak expiration). At this time instant, the flow predominantly occurs in the direction G5-G0. The velocity fields presented in Fig. 15 for the out-of-plane configuration show significant qualitative and quantitative

differences from those in Fig. 7 for the in-plane configuration. The primary velocity contours at the end planes of G2 and G3 branches for the out-of-plane configuration (Fig. 15) show a cross-shaped region of high expiratory velocity in the center of the cross section as compared to the relatively larger elongated regions of high velocity observed for the in-plane configuration (Fig. 7). Figure 15 shows that the patterns of secondary flow at G1P1 for the out-of-plane configuration comprises four vortices as compared to the eight vortices observed at the same location for the in-plane configuration. Although regions of oppositely directed (inspiratory) flow of relatively small magnitudes are seen at peak expiration in the branches of generations G2-G0 of the out-of-plane configuration as was found for the in-plane configuration, their extents are appreciably different in the two cases. (No bidirectional flow is observed at this time instant in generations G3, G4, or G5. There is no bidirectional flow at peak expiration in the pipe solution of Womersley.¹⁸)

While the cross-sectional distribution of the primary velocity at the end planes of the branches of generations G1-G3 for the out-of-plane configuration show significant asymmetry at peak inspiration (Fig. 13), peak expiration (Fig. 15) is characterized by more symmetric velocity distributions. Such reduced asymmetry in the velocity contours during expiration was also observed in Fig. 7 for the in-plane configuration. This reduced asymmetry in the cross-sectional flow field thus displays the fundamental difference between the fluid dynamics of successively bifurcating flow and that of successively combinatory flow.

The velocity fields at the end planes of the branches of generations G0-G3 at $t = T$ (end of expiration/beginning of inspiration) are shown in Fig. 16. As in Fig. 14 ($t = T/2$), the flow in the branches of generations G0-G3 at $t = T$ (Fig. 16) are characterized by bidirectional flows, the magnitudes of primary velocity in the two directions being of similar strengths. As explained previously, the nonuniform flow structures seen in Fig. 16 are entirely due to the

unsteady effects since a steady flow solution with the same boundary condition would have resulted in zero velocity everywhere in the flow field. A comparison of Figs. 14 and 16 shows that the distribution of the primary velocity over the cross section is quite different at the two time instants. While the inspiratory flow occurred in the central region with expiratory flow in the peripheral regions at $t = T/2$, the inspiratory flow is restricted to the peripheral regions while the expiratory flow occupies central regions at $t = T$. This may be attributed to the effects of inertia of the flow. At the end of inspiration ($t = T/2$), the flow in the central regions of the cross section is dominated by the inertia of inspiratory flow, while that near the walls begin to show expiratory flow features; the reverse happens at the end of expiration ($t = T$). The range of velocity magnitude (negative to positive) at $t = T$ is the greatest in G0 and its value is progressively lower in G1, G2, G3 and so on. As explained previously, this reduction in range in velocity (i.e., amplitude) is caused by a reduction in Womersley number down the generations. The secondary flow patterns at all the cross-sectional planes shown in Fig. 16 for $t = T$ are characterized by four vortices, similar to that observed at peak expiration. Thus, the secondary flow field is related to the secondary flow structure occurring in the preceding part of the cycle.

While the cross-sectional velocity distribution at different location in generations G0-G3 of the out-of-plane configuration were shown in Figs. 13–16, the following four figures show the three-dimensional evolution of the velocity field in the G0-G5 network during a breathing cycle. The colors represent the magnitude of velocity, while the direction is borne by the orientation of the vectors themselves. These three-dimensional vector plots provide complementary information regarding the flow structures which were not revealed in Figs. 13–16. Only this information is presented below for the sake of brevity.

Figure 17 shows the velocity vector plots at the end planes of the branches of generations G1-G5 at $t = T/4$ (peak inspiration). A comparison of Figs. 17 and 9 shows that at peak inspiration, the nonuniformity of flow distribution among the branches of a particular generation is significantly smaller for the

out-of-plane configuration as compared to that for the in-plane configuration.

The velocity vectors at the end planes of the branches of generations G1-G5 at $t = T/2$ (end of inspiration/beginning of expiration) are shown in Fig. 18. The simultaneous existence of inspiratory and expiratory flow may be attributed to flow inertial effects, as explained previously. The amplitude of velocity variation is the greatest in G0 and its value is progressively lower in G1, G2, G3, and so on. This reduction is caused by a reduction in Womersley number down the generations. Figure 18 shows that the nonuniformity in flow distribution among the branches of generation G5 is small, with the region of inspiratory flow (positive primary velocity) shifting toward the center of the cross section as one traverses from G3 to G5. A comparison of Figs. 10 and 18 shows that although the flow field is almost unaffected by the configuration of branches up to the end plane of generation G1, the nonuniformity in the distribution of flow among the branches of a particular generation is significantly reduced in the out-of-plane configuration beyond generation G1.

Figure 19 shows the velocity vectors at the end planes of the branches of generations G1-G5 at $t = 3T/4$ (peak expiration) for the out-of-plane configuration. The present computation reveals that the velocity distributions have four peaks in G0, four in G1, two peaks (though not well-defined) in G2, followed by a single peak in generation G3 onward. This variation is in contrast to the existence of a single peak in all generations at peak inspiration (for both in-plane and out-of-plane configurations), and to the existence of four peaks (which merge along the straight length of a branch to give a plateaulike distribution) in all generations at peak expiration for the in-plane configuration (Fig. 11).

Figure 20 shows the velocity vectors on the end planes of branches of generations G1-G5 at $t = T$ (end of expiration/beginning of inspiration). The simultaneous existence of inspiratory and expiratory flow may be attributed to flow inertial effects, as explained previously. The amplitude of velocity variation is the greatest in G0 and its value is progressively lower in G1, G2, G3 and so on. This reduction is caused by a reduction in the Womersley

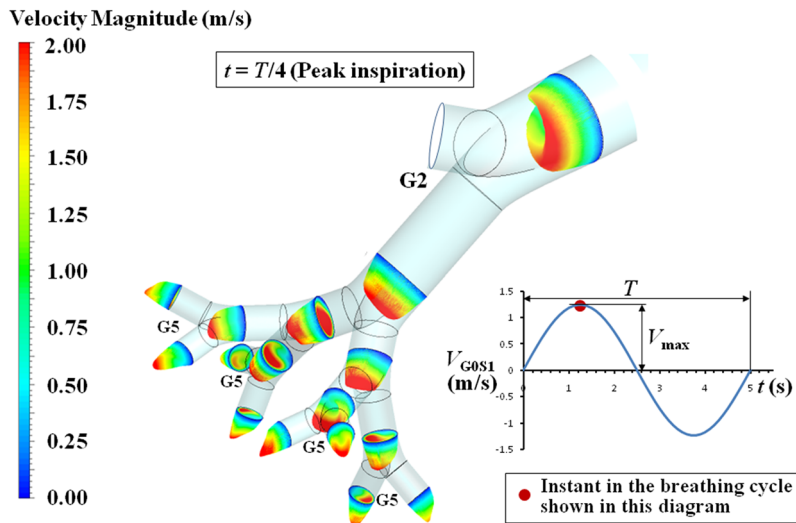


FIG. 17. The vectors of velocity at selected cross-sectional planes showing the three-dimensional evolution of the flow field at peak inspiration; out-of-plane configuration.

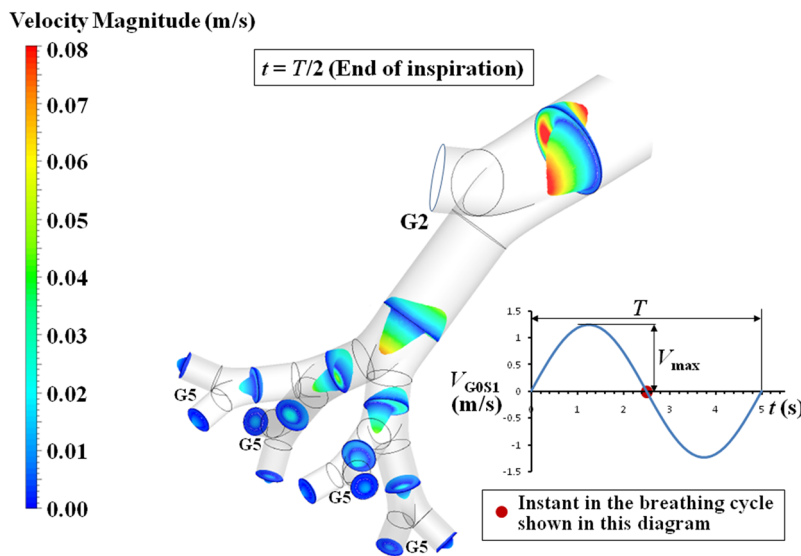


FIG. 18. The vectors of velocity at selected cross-sectional planes showing the three-dimensional evolution of the flow field at the end of inspiration; out-of-plane configuration.

number down the generations. It is interesting to note that the level of nonuniformity in the flow distribution among the branches of a particular generation is much smaller at the end of expiration (Fig. 20) as compared to that at the end of inspiration (Fig. 18). This may be attributed to the smaller asymmetry in the flow distribution during the expiratory phase as compared to that during the inspiratory phase.

The present computations reveal that bidirectional flow exists at both time instants $t = T/2$ and $t = T$, but there are differences in the details of the velocity distribution. At $t = T/2$, one inspiratory peak and one expiratory peak are observed at a cross section. At $t = T$, two expiratory peaks and two inspiratory peaks are observed, though all peaks are not well-defined. This difference is the manifestation of different degrees of cross-sectional flow asymmetry developed in the respective preceding part of the cycle.

B. Temporal evolution of the flow field: Quantification of “unsteady effects”

Until now, we have discussed about the evolution of the velocity field as the flow traverses from generation G0 to G5 (during inspiration) or from G5 to G0 (during expiration) at some particular instants in the breathing cycle. Now, we focus on the temporal evolution of the flow field at a fixed location in the branching network during a complete breathing cycle. Results for the in-plane configuration only are reported below to save space. In the present study, we have considered a breathing rate of 12/min which corresponds to a breathing cycle time period (T) of 5 s. We have carefully analyzed the data of a breathing cycle at intervals of $T/10$ s, but presented the data only at $t = T/10$, $t = 4T/10$, $t = 5T/10 = T/2$, $t = 6T/10$, $t = 9T/10$, and $t = 10T/10 = T$ in Figs. 21 and 22 to keep

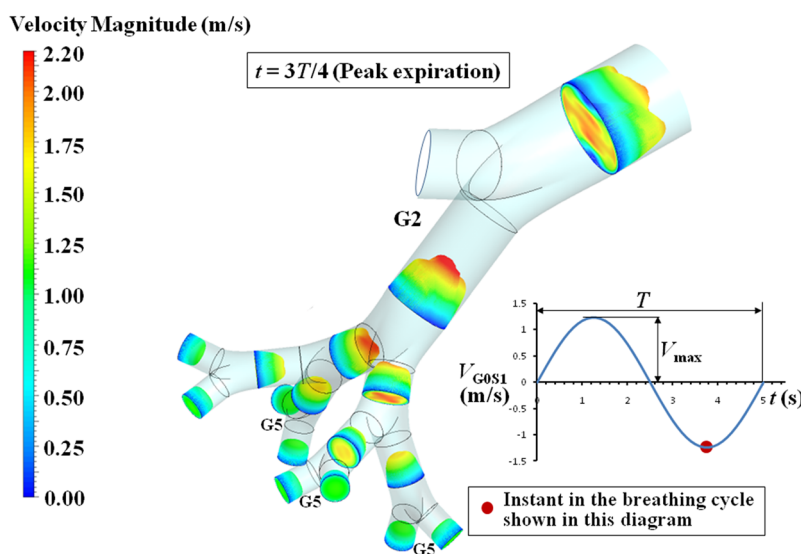


FIG. 19. The vectors of velocity at selected cross-sectional planes showing the three-dimensional evolution of the flow field at peak expiration; out-of-plane configuration.

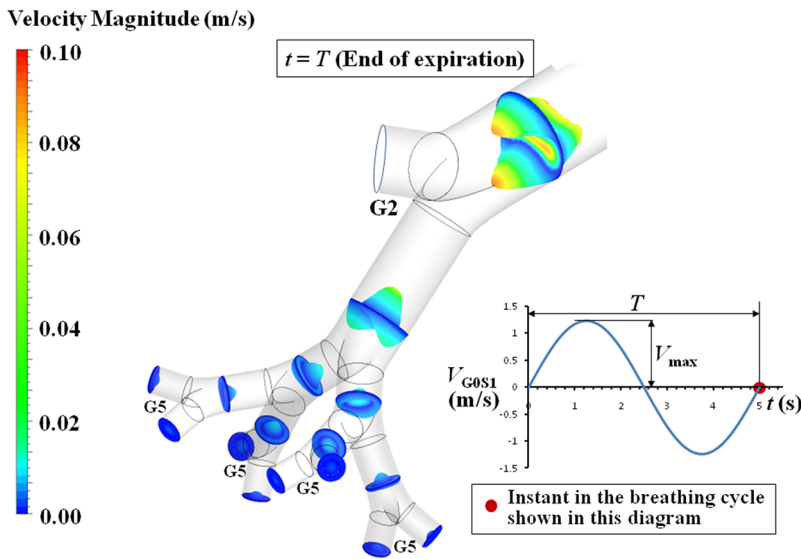


FIG. 20. The vectors of velocity at selected cross-sectional planes showing the three-dimensional evolution of the flow field at the end of expiration; out-of-plane configuration.

them uncluttered. Additionally, the velocity data at peak inspiration ($t = T/4$) and peak expiration ($t = 3T/4$) are included. In the inspiratory phase of the breathing cycle, the flow at plane G0S1 accelerates during $t = 0$ to $t = T/4$ (peak inspiration) and decelerates from $t = T/4$ to $t = T/2$ (Fig. 3). Thus, although the magnitudes of velocity at the boundary of the first generation (G0S1) of the network at $t = T/10$ and at $t = 4T/10$ are equal, the flow at G0S1 is accelerating at $t = T/10$, while it is decelerating at $t = 4T/10$. Again, in the expiratory phase, the flow accelerates during $t = T/2$ to $t = 3T/4$ (peak expiration) and decelerates from $t = 3T/4$ to $t = T$.

In addition to the unsteady simulation covering the entire breathing cycle, separate steady state solutions are run at each selected time instant (with the same boundary condition at G0S1 at the same time instant as is employed in the unsteady simulation) in order to determine by what extent the unsteady solutions differ from their steady flow counterparts. Figure 21 shows the variation of the primary velocity v_p along a diameter lying on the meridional plane at the plane G1P1. The primary velocity during the inspiratory phase shows a skewed nature with the maximum shifted toward the inner edge of the preceding bifurcation. The unsteady and steady solutions at $t = T/4$ nearly coincide thus leading to the conclusion that the quasisteady approximation is valid at peak inspiration. Although not plotted, the velocity profiles at $t = 2T/10$ and $t = 3T/10$ (when the

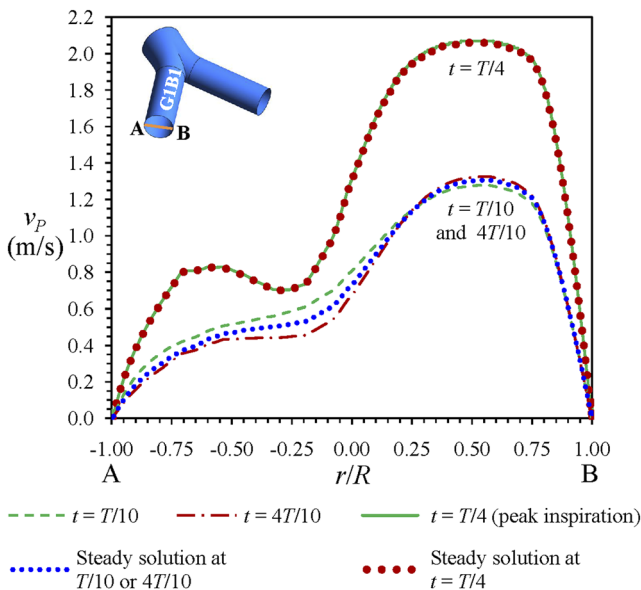


FIG. 21. Variation of the primary velocity at plane G1P1 along the diameter AB which lies on the meridional plane at different time instants during the inspiratory phase; in-plane configuration.

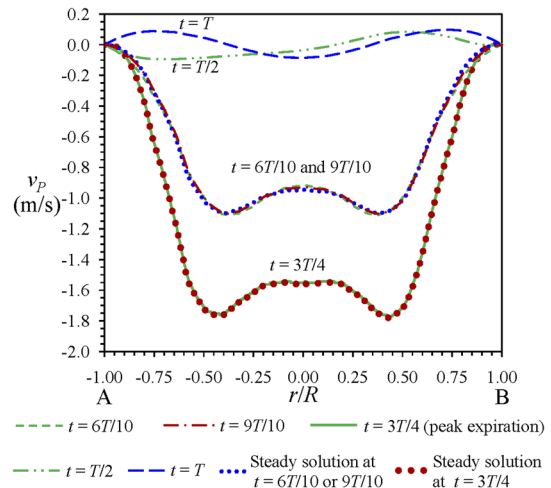


FIG. 22. Variation of the primary velocity at plane G1P1 along the diameter AB which lies on the meridional plane during the expiratory phase and at instants of changeover ($t = T/2$, $t = T$); in-plane configuration.

prescribed velocity at the boundary G0S1 are equal) nearly overlap indicating that unsteady effects are limited near the peak inspiration point ($t = T/4$). Similarly, the time instants $t = T/10$ and $t = 4T/10$ are selected such that the magnitudes of velocity at the G0S1 at these time instants are equal, and one instant falls within the accelerating part and the other instant falls within the decelerating part of inspiratory flow. The two steady solutions at these two instants are identical since the boundary condition remains the same. Figure 21 shows that there are considerable differences between the unsteady solution at $t = T/10$, unsteady solution at $t = 4T/10$ and the common steady solution. These (asymmetric) differences signify a method of quantification of the unsteady flow effect in a branching network. According to the theories of Sexl,¹⁵ Lambosy,¹⁷ and Womersley¹⁸ for the oscillating fully developed flow in a pipe, velocity contours at any time instant are concentric circles and the above-mentioned unsteady effect is axisymmetric (i.e., not a function of the cylindrical coordinate θ). This symmetry in space is destroyed in the present solutions, the nonuniformity displayed in Figs. 5, 6, 13, and 14 bearing testimony to that. Thus, the asymmetry in the unsteady effects during inspiration is peculiar to the oscillating flow in a branched network.

Figure 22 shows that the primary velocity during the expiratory phase possesses an M-shaped profile which is approximately symmetric about the center of line AB. The unsteady solution and the steady solution nearly coincide at $t = 3T/4$, thus leading to the conclusion that the quasisteady approximation is valid at peak expiration. It is further seen that there is little difference between the unsteady solution at $t = 6T/10$, the unsteady solution at $t = 9T/10$ and the common steady solution. Similar behavior occurs at other instants during the expiration phase. It is thus concluded that the unsteady effects are not significant during the entire duration of expiration through an elaborate network at the Womersley number of simulation (2.64 at generation G0). This considerable difference in the unsteady effects during inspiration and that during expiration is peculiar to the branching network, since, according to the theories of Sexl,¹⁵ Lambosy,¹⁷ and Womersley¹⁸ for the oscillating fully developed flow in a pipe, the magnitude of unsteady effect at a time instant during inspiration is identical to the same at a corresponding time instant during expiration. This symmetry in time is also destroyed in the present solutions.

Figure 22 also shows the unsteady solutions at $t = T/2$ and at $t = T$. The steady flow solutions at these two instants give zero velocity everywhere since the prescribed velocity at the boundary G0S1 is zero. Both unsteady solutions consist of bidirectional flow (there are regions of a cross section where flow occurs in the direction G0 to G5, the flow occurring in the opposite direction, i.e., from G5 to G0, over the rest of the cross section) as is predicted in the theoretical work of Sexl,¹⁵ Lambosy,¹⁷ and Womersley¹⁸ for the oscillatory fully developed flow in a pipe. However, unlike the flow in pipe, the two unsteady solutions for the branching network, particularly the solution at $t = T/2$, are not symmetric with respect to the radius (i.e., not axisymmetric) and are not mirror images to one another. Since the flow structure at an instant is shown to be related to that in the preceding part of the cycle, the greater symmetry in the profile at $t = T$ is caused by the greater symmetry found in the expiratory phase as compared to the inspiratory phase. Since the steady flow solutions at these two instants would predict no flow at all, it is concluded that the unsteady effects are at their maximum during the changeover

from expiration to inspiration ($t = 0$ or $t = T$) and inspiration to expiration ($t = T/2$).

When the flow solution is analyzed along a diameter CD which is perpendicular to AB shown in Figure 21, it is found that the primary velocity during both the inspiratory and expiratory phases shows an M-shaped profile which is approximately symmetric about the center of CD. The unsteady effects on the velocity profiles along CD at various instants of the breathing cycle show similar general behaviors as are discussed above for velocity profiles along AB. The results of the computation at various other branches are also analyzed in the same manner as above, though these are not plotted to save space. It is found that unsteady effects, in the sense described above, diminish in the direction G0 to G5. This is consistent with the fact that the local Womersley number diminishes in the direction G0 to G5 with progressively smaller branch diameters.

Figure 23 shows the variation with time of the average velocity through a particular branch \bar{V}_{branch} . It may be interpreted as the area-averaged velocity.^{52,53} When \bar{V}_{branch} is multiplied with the cross-sectional area of the branch, one obtains the net volume flow rate through the same branch. Instead of plotting the time variation of average velocity in all of the 63 branches present in the network, which will make the figure cluttered, we have selected those branches in the six generations such that the branches lie either on the maximum flow path or the minimum flow path at peak inspiration. The maximum flow path consists of the branches G0B1-G1B1-G2B2-G3B3-G4B6-G5B11. The minimum flow path consists of the branches G0B1-G1B1-G2B1-G3B1-G4B1-G5B1. It is found that the difference in \bar{V}_{branch} between the two selected branches of any generation (G2B2 and G2B1, G3B3 and G3B1, G4B6 and G4B1, and G5B11 and G5B1) during the inspiratory phase is significant and the difference increases with increasing generation number (this is consistent with the variation of δ_{Gn} described later in Sec. IV D). The corresponding difference in each generation during the

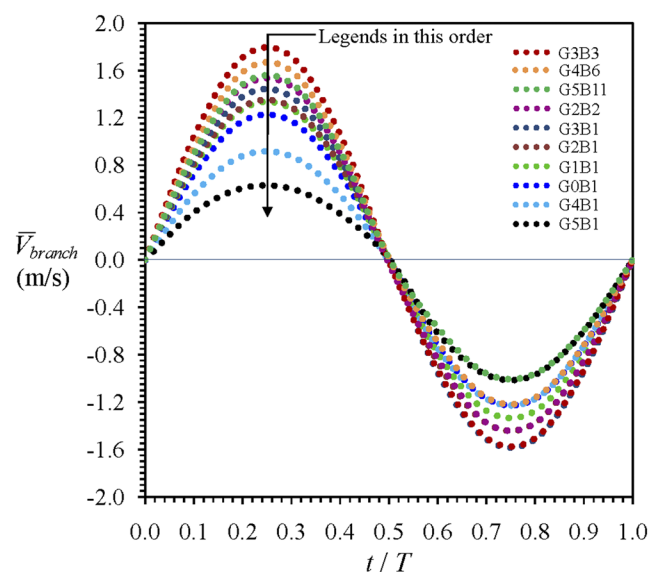


FIG. 23. Variation of the average velocity in various branches with time; in-plane configuration.

expiratory phase is very small. This shows that the mass flow distribution between various branches of a generation is nearly uniform during expiration. During inspiration, \bar{V}_{branch} in a particular branch in a specific generation depends on two factors—the change of branch diameter with generation and the asymmetry of mass flow distribution among the various branches (all of same diameter) of a particular generation. It is for these two factors that \bar{V}_{branch} in G2B2 and G5B11, and, \bar{V}_{branch} in G2B1 and G1B1 are close during the inspiratory phase.

C. Spatial evolution of the secondary flow field at peak inspiration and expiration

In a branching network, the curvature of the flow path in the bifurcation module, flow division at the bifurcation ridge, and complex change of cross-sectional shape and area as the mother branch divides into two daughter branches gives rise to a secondary flow field. In addition to this, the repeated switch-over from clockwise to anticlockwise curvature and vice versa in the flow path also considerably affect the secondary flow field. A detailed account of the secondary flow field in a branching network may be found in Ref. 2. The changes in the secondary flow field across a bifurcation as well as that across the straight section following a bifurcation were illustrated in that paper. General qualitative features of secondary flow pattern at four characteristic time steps of oscillatory flow are discussed in previous sections of this paper—in Figs. 5–8 for in-plane configuration and in Figs. 13–16 for out-of-plane configuration. In this section, we compare the evolution of the secondary flow field quantitatively during peak inspiration and peak expiration for the two configurations (in-plane and out-of-plane). It is to be noted that the positions of the vortices are identified by using the λ_2 criterion⁵¹ in addition to a visual inspection of the secondary flow patterns at the

cross section. In addition to the contours and flow patterns, the values of average secondary velocity $\bar{v}_s (\equiv \sqrt{\int |\vec{v}_s|^2 dA / \pi R^2})^2$ at a cross section are also quoted to indicate the variation of the secondary flow strength along the flow direction.

Figure 24 shows the secondary velocity vectors superposed on the contours of secondary velocity magnitude at plane GOP1 and those at equidistant planes between the start plane (G1S1) and end plane (G1P1) of G1B1 for the in-plane configuration. The adopted representational convention is such that the bifurcation ridge just downstream of the concerned cross-section appears as a vertical line in the diagram. During inspiration, the predominant direction of motion of fluid is from G0 to G2 and the flow divides at each bifurcation module into two streams. For this configuration, the secondary velocity field is symmetric about a horizontal centerline in the diagram (i.e., the longitudinal symmetry plane¹). The characteristics of the secondary flow field at peak inspiration are qualitatively similar to those reported in Ref. 2 for steady flow at a comparable Reynolds number. A comparison of the flow patterns and \bar{v}_s values at planes GOP1 and G1S1 illustrates the changes caused by the bifurcation module: a significant increase of secondary flow magnitude, and the development of Dean-type circulation. As the fluid travels along the straight portion of branch G1B1, the magnitude of the secondary velocity (indicated by the quoted values of \bar{v}_s) decreases considerably and the locations of the maximum secondary velocity tend to shift from a central region to near the top and bottom walls. The cores of the Dean vortices, on the other hand, tend to shift from the peripheral regions on the plane G1S1 to more central regions on the plane G1P1. Similar changes in the secondary flow pattern are also found (not shown here) to occur across the straight portions of branches G2B1 and G2B2. In spite of these changes, the basic flow structure (i.e., number of vortices and sense of rotation

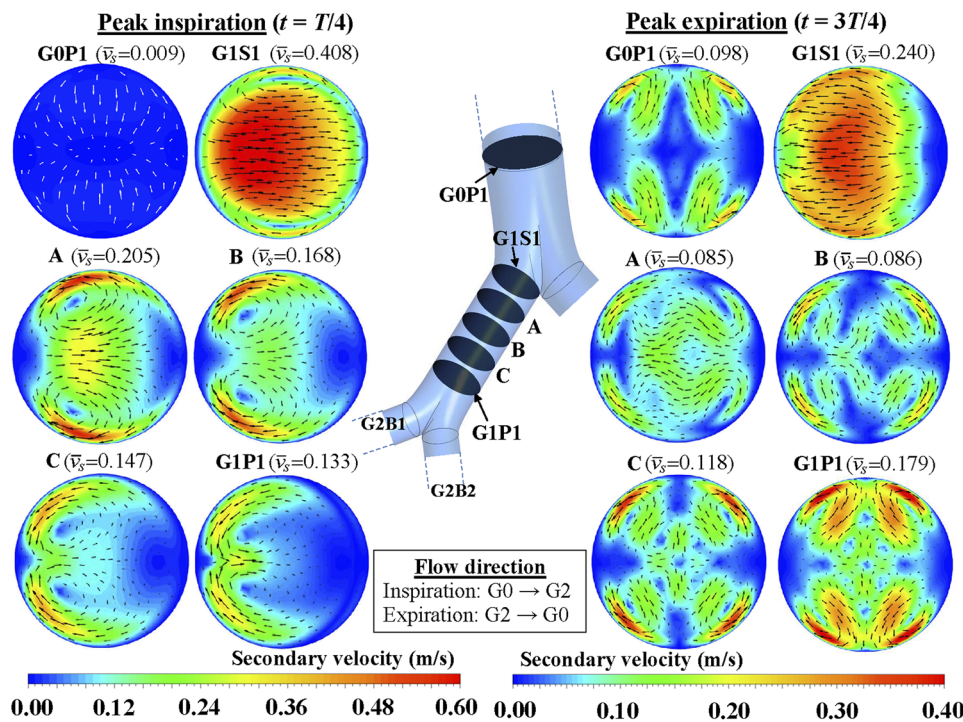


FIG. 24. Secondary velocity vectors superposed on the contours of secondary velocity magnitude at numerous cross-sectional planes in branch G1B1 during peak inspiration and peak expiration; in-plane configuration.

in the vortices) remains unaltered across the straight portion of a branch.

During expiration, the predominant flow direction is from G2 to G0 and the flow streams from two branches of generation Gn unite in a branch of generation $Gn - 1$. It is found in Fig. 24 that the secondary flow at G1P1 (which is the start plane of G1B1 during expiration) is characterized by four pairs of vortices and maximum velocity near the top and bottom walls. As the fluid traverses along the straight portion from G1P1 to G1S1, the secondary flow strength decreases up to plane A, and the vortices seem to disappear from the cross section. The combination of the two streams coming from G1B1 and G1B2 is felt upstream of the bifurcation module and the streamlines at plane G1S1 itself are significantly bent, with corresponding increase in the value of \bar{v}_s there, as evidenced in Fig. 24. This explains the increased intensity of secondary motion directed away from the inner edge of the bifurcation at G1S1. A comparison of the secondary flow at G1S1 and G0P1 during expiration shows that the bifurcation module regenerates vortical secondary motion, giving rise to four vortices at plane G0P1. However, the magnitude of \bar{v}_s is smaller at G0P1 as compared to that at G1S1. This may be understood from the much gentler local curvature of the flow at G0P1 as compared to that at G1S1.

While Fig. 24 applies to the in-plane configuration, Fig. 25 highlights the corresponding scenario for the out-of-plane configuration, showing the secondary velocity vectors superposed on the contours of secondary velocity magnitude at planes G0P1, G1S1, G1P1, and G2S1 during peak inspiration and peak expiration. At peak inspiration, the characteristics of the secondary flow field are qualitatively similar to those reported in Ref. 2 for steady flow at a comparable Reynolds number. A comparison between the flow patterns and \bar{v}_s

values (given in Fig. 25) at plane G0P1 and those at G1S1 (and that between G1P1 and G2S1) illustrates the changes caused by the bifurcation module, while the differences between the secondary flow at planes G1S1 and G1P1 depict the changes across a straight section. At peak inspiration, the value of \bar{v}_s increases across a bifurcation module due to the introduction of fresh secondary motion. Moreover, the qualitative nature of the secondary flow pattern may be altered altogether. As an example, it is observed that the two-vortex flow pattern at G1P1 changes to a three-vortex pattern at G2S1. On the other hand, the straight section of a branch only attenuates secondary flow strength without affecting the qualitative nature of the vortex pattern.

During peak expiration, the secondary flow pattern in the out-of-plane configuration (Fig. 15) is characterized by a four-vortex system at the GnP_k planes for branches of generations G0-G3. This is significantly different from the two or three-vortex secondary flow patterns observed during peak inspiration in the same branching network (Fig. 13). Figure 25 shows that the secondary velocity distributions (i.e., the contours of secondary velocity magnitude) in the G0-G2 branches are considerably different from those during peak inspiration. This may be attributed to the location of the selected cross-sectional planes with respect to the inlet of the network; while plane G0S1 is the inlet to the network during inspiration, the planes G5Pk (where $k = 1, 2, 3, \dots, 32$) are the inlets to the network during expiration. As an example, during peak inspiration, the flow does not encounter any bifurcation module up to plane G0P1 and hence only small values of secondary velocity are found at that plane. On the other hand, during expiration, the same plane is reached by the flow after traversing several generations and bifurcation modules and hence comparatively greater secondary velocities are observed there.

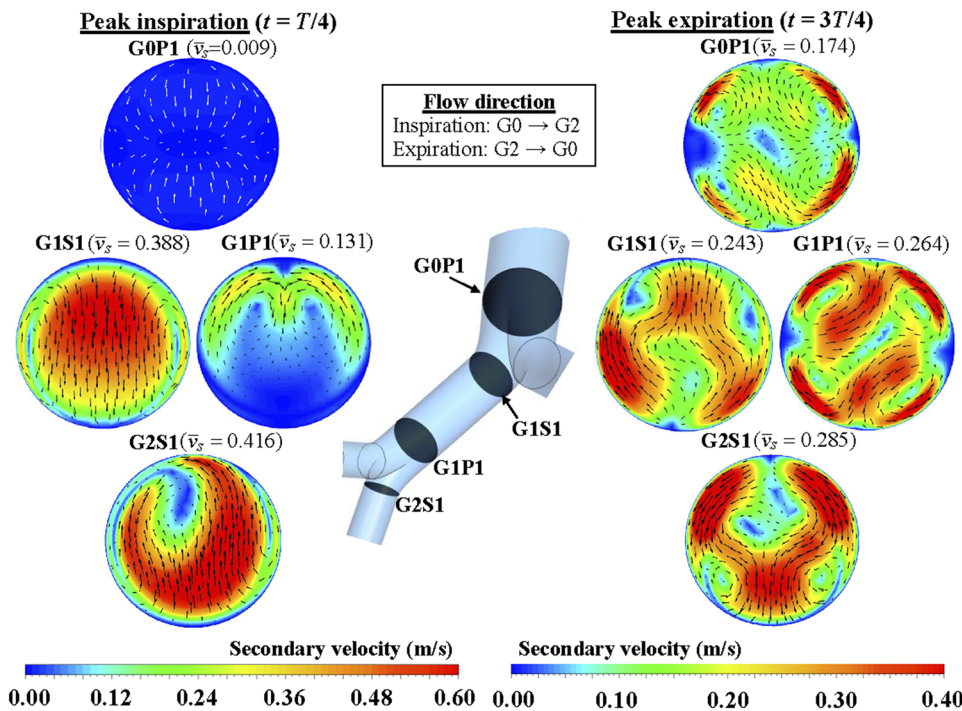


FIG. 25. Secondary velocity vectors superposed on the contours of secondary velocity magnitude at selected cross-sectional planes in generations G0-G2 during peak inspiration and peak expiration; out-of-plane configuration.

In contrast to the observation made for peak inspiration, it is found that during peak expiration qualitative changes in the secondary flow pattern may occur along the straight section of a branch (such as the change of the four-vortex system at G1P1 to a two-vortex pattern at G1S1).

The effects of the three-dimensional arrangement of the branches on the secondary flow can be studied by comparing the solutions for in-plane and out-of-plane configurations. During peak inspiration, the secondary velocity field is qualitatively similar in either configuration up to the end plane of the branches of generation G1. However, from generation G2, the secondary flow pattern in the out-of-plane configuration (Fig. 13) is significantly different from that in the in-plane configuration (Fig. 5). For example, the secondary flow pattern at G2P1 is characterized by a four-vortex system for the in-plane configuration, whereas a three-vortex flow pattern is observed at a similar location in the out-of-plane configuration. It has been established in Ref. 2 that, during peak inspiration, the secondary flow strength (indicated by \bar{v}_s) is greater in out-of-plane configuration than that at a corresponding location in in-plane configuration, the difference being appreciable as one focuses attention to higher generation number G_n . This may be attributed to the more tortuous flow path in the out-of-plane configuration. Figures 24 and 25 demonstrate that, during peak expiration, this (i.e., the fact that \bar{v}_s has a greater magnitude in out-of-plane configuration) is true even at planes G0P1 and G1P1. The secondary velocity contours for the in-plane configuration in Fig. 24 (for both peak inspiration and peak expiration) are symmetric about a horizontal centreline in the diagram. For the out-of-plane configuration, although a line of symmetry is observed up to plane G1P1 during peak inspiration, no line of symmetry exists during peak expiration.

D. Spatial and temporal evolution of the flow asymmetry

Figure 26 shows the velocity distribution on the meridional plane (a plane passing through the center of the geometry and

containing the centerlines of all the generations) at peak inspiration ($t = T/4$) and peak expiration ($t = 3T/4$). Inspiratory flow velocities are considered positive while expiratory flow velocities are considered negative. As the length of G0B1 is smaller than the entrance length (corresponding to the Reynolds number for peak inspiration), the velocity profile is still developing when the first bifurcation is reached during inspiration. Although the velocity distributions in branches G1B1 and G1B2 are mirror images of one another, the combined effects of flow path curvature and flow inertia result in the velocities becoming skewed with maxima near the inner edges of the preceding bifurcation.¹ As a result of this skewed velocity distribution in the G1 branches, the maximum (and average) velocity in branch G2B2 is found to be significantly greater than that in branch G2B1. This characteristic of the mass-flow distribution, whereby the branch (say, G2B2) aligned with its grandmother (G0B1) shows greater maximum (and average) velocities than its sister branch (G2B1), is found to be generically true for all dichotomously branching networks. Due to the above-mentioned generic flow distribution characteristic, the maximum (and average) velocity is the greatest in branch G3B3 (in generation G3), G4B6 (in generation G4) and G5B11 (in generation G5). Thus, the velocity distribution on the meridional plane at peak inspiration shows that even for the geometrically symmetric network there exists significant asymmetry in the mass flow distribution.

The velocity contours on the meridional plane at peak expiration shown in Fig. 26 reveal that the flow distribution at any generation is much more symmetric as compared to that during inspiration. During expiration, as the flow traverses a bifurcation joining two branches of generation G_n to a branch of generation $G_n - 1$, the curvature of the flow path pushes the maximum velocity toward the center of the cross-section in the $G_n - 1$ branch. This results in more uniform velocity distribution in the $G_n - 1$ branch leading to a reduction in the asymmetry in the mass flow distribution among the branches lying further downstream. Thus, flow division at a bifurcation during inspiratory flow generates nonuniformity in

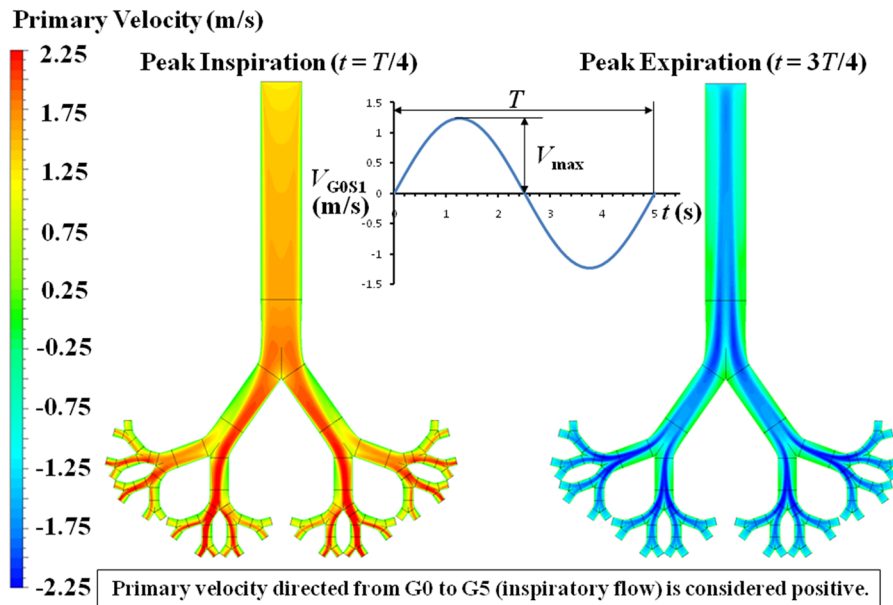


FIG. 26. Contours of primary velocity on the meridional plane (which contains the centerlines of all the branches) during peak inspiration and peak expiration; in-plane configuration.

the flow distribution, whereas flow combination at the same bifurcation during expiratory flow tends to increase symmetry in the flow field. Figure 26 vividly demonstrates this essential irreversibility of fluid dynamics.

In the branching network considered in the present study, the total flow area decreases from generation G0 to G3 and then increases from G3 to G5. Hence, for a given mass flow rate at the boundary of the first generation, the average velocity is greatest in generation G3 at both peak inspiration and peak expiration. Due to the greater symmetry in the mass flow distribution in branches of a generation during expiration, the maximum velocity during peak expiration also occurs in generation G3. However, the mass flow distribution is highly asymmetric during peak inspiration and the asymmetry grows in downstream generations (see below). As a consequence, the maximum velocity during peak inspiration occurs in G5—the last generation of the adopted network.

It was shown in Ref. 1 that even though a mother branch divides to give rise to two identical daughter branches at each bifurcation of the symmetric network, the mass flow entering the two daughters at a bifurcation during steady inspiratory flow are unequal from generation G2 onward for the in-plane configuration and from G3 onward for the out-of-plane configuration. We have therefore plotted the values of $\dot{m}_{G2B1}/\dot{m}_{G2B2}$, $\dot{m}_{G3B1}/\dot{m}_{G3B2}$, and $\dot{m}_{G3B3}/\dot{m}_{G3B4}$ for the in-plane configuration, and $\dot{m}_{G2B1}/\dot{m}_{G2B2}$, $\dot{m}_{G3B1}/\dot{m}_{G3B2}$ for the out-of-plane configuration at different instants of the breathing cycle in Fig. 26. The deviation of the ratio of mass-flow rates for two sister branches from unity quantifies the level of asymmetry in the mass-flow distribution. It is found that significant asymmetry in the mass-flow distribution exists during the inspiratory phase while the mass-flow distribution becomes almost uniform during the expiratory phase. Moreover, the asymmetry in the mass-flow distribution at all-time instants is significantly smaller for the out-of-plane configuration as compared to that in the in-plane configuration.

Figure 27 shows that the level of asymmetry for branches G3B3 and G3B4 is greater than that for branches G3B1 and G3B2 in the in-plane configuration. It was also found that in generation G4, the level of asymmetry is greatest for branches G4B5 and G4B6. It has been established¹ that during the inspiratory phase, the maximum mass-flow rates occur along the path G0B1-G1B1-G2B2-G3B3-G4B6-G5B11. From this and many other similar considerations, it is concluded that in a particular generation, the greatest level of asymmetry usually involves that branch which has the maximum mass-flow rate in that generation.

A new concept called “degree of mass-flow asymmetry” (δ_{Gn}) was introduced in Ref. 1 as a simple quantitative measure of the nonuniformity in the mass flow rates in various branches of a particular generation. It is defined as follows:

$$\delta_{Gn} \equiv (\dot{m}_{Gn,max} - \dot{m}_{Gn,min}) / \dot{m}_{Gn,avg}, \quad (6)$$

where $\dot{m}_{Gn,avg} = \frac{1}{2^n} \sum_{k=1}^{k=2^n} \dot{m}_{Gn,k}$ is the average mass flow rate per branch in a generation and, $\dot{m}_{Gn,max}$ and $\dot{m}_{Gn,min}$ are, respectively, the maximum and minimum mass flow rates in that generation. Figure 28 shows the evolution of the degree of mass flow asymmetry (δ_{Gn}) in successive generations of the G0-G5 network when the branches are arranged according to the in-plane configuration.

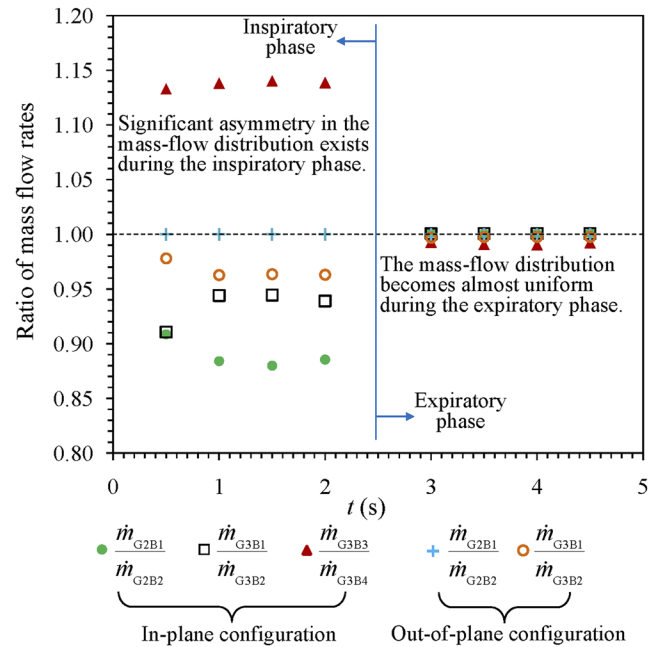


FIG. 27. Temporal variation of the asymmetry in mass-flow distribution among the branches of generations G2 and G3.

The value of δ_{Gn} is zero for generation G1 due to the symmetry of the flow field.¹ δ_{Gn} during the inspiratory phase is about an order of magnitude greater than that during the expiratory phase. Moreover, δ_{Gn} increases as the flow traverses from generation G2 to G5

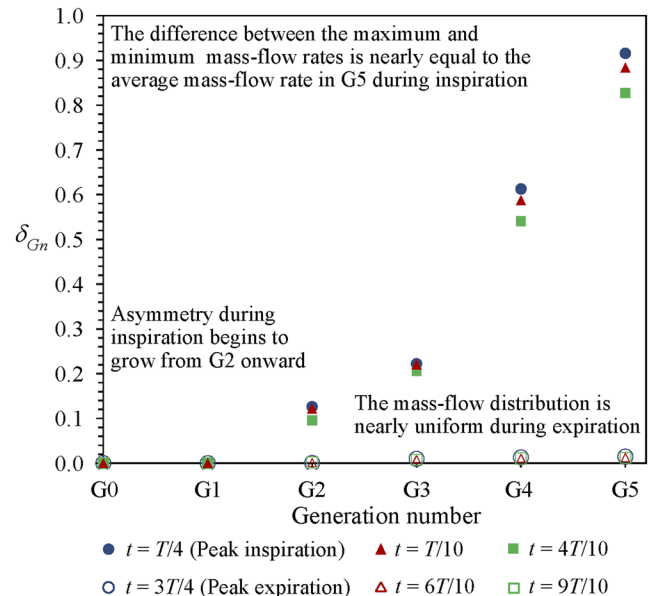


FIG. 28. Spatial evolution of the degree of mass-flow asymmetry with increasing generation number at various instants of the breathing cycle; in-plane configuration.

during inspiration, with values close to unity at G5. This indicates that the difference between the maximum and minimum mass flow rates is almost equal to the average mass flow rate in generation G5 during inspiration. Another interesting observation that may be made from Fig. 28 is that from generation G2 onward, the value of δ_{Gn} at peak inspiration is greater than that at other instants of the inspiratory phase. Moreover, the difference between δ_{Gn} values at $t = T/10$ (acceleration phase) and $t = 4T/10$ (deceleration phase) increases down the generations indicating that the unsteady effects increase down the generations during inspiration. The value of δ_{Gn} is found to be significantly smaller during the expiratory phase. As an example, at generation G5, δ_{Gn} is about two orders of magnitude greater during inspiration than that during expiration.

Figure 29 shows the evolution of δ_{Gn} down the generations in the out-of-plane configuration of G0-G5 network. $\delta_{Gn} \cong 0$ up to generation G2 owing to the symmetry of the flow field for this configuration.¹ The value of δ_{Gn} at a particular generation for this configuration is found to be significantly smaller than that for the in-plane configuration. As for the in-plane configuration, the value of δ_{Gn} is found to be significantly smaller during the expiratory phase. However, owing to the smaller values of δ_{Gn} itself for the out-of-plane configuration, the variation of δ_{Gn} over a complete breathing cycle is smaller for this configuration.

E. Effects of Womersley number on the unsteady flow in 3D branching networks

All solutions up to Sec. IV D correspond to the breathing cycle at the resting condition in humans ($\alpha_{G0} = 2.64$ in the trachea). However, in many practical cases (physical stress, artificial respiration), the Womersley number (α) might be higher. Various values of the Womersley number may also be relevant for future engineered

branching networks. In the case of high frequency oscillatory ventilation (HFOV), a much higher value of frequency f and a much higher value of tidal volume per unit time (than the normal human breathing condition) are employed, which would change both Re_{max} and α_{G0} simultaneously. In order to obtain additional insight on the isolated role of the Womersley number on the unsteady fluid dynamics in a branching network, an additional unsteady simulation is performed at $\alpha_{G0} = 10$, keeping the same in-plane geometry of the branching network, same properties of the fluid and the same maximum inlet Reynolds number ($Re_{max} = 1522$). The change in α_{G0} is thus achieved in the computation by changing the frequency f resulting in a time period of $T = 0.35$ s. Salient aspects of this additional simulation are given in this section. The use of the same Re_{max} ensures that the steady solutions at peak inspiration and peak expiration remain the same as discussed in previous sections.

Figures 30 and 31 confirm that the previous conclusion (made in Sec. IV B) that the quasisteady approximation is valid at peak inspiration as well as at peak expiration is valid even at a value of α_{G0} as high as 10. A comparison of Fig. 30 with Fig. 21 shows that the velocity curve at peak inspiration is basically unaltered and the unsteady effect (the difference between the unsteady solution at $t = T/10$ and that at $t = 4T/10$) is appreciably increased as the Womersley number α_{G0} increases from 2.64 to 10. In contrast to the oscillating fully developed flow in a straight pipe,¹⁵⁻¹⁸ where the velocity contours at any time instant are concentric circles and the above-mentioned unsteady effect is axisymmetric, the spatial asymmetry in the unsteady effects during inspiration is peculiar to the oscillating flow in a branched network.

A comparison of Figs. 31 and 22 shows that the increased value of α leads to greater differences between the unsteady solution at $t = 6T/10$, that at $t = 9T/10$, and their corresponding steady

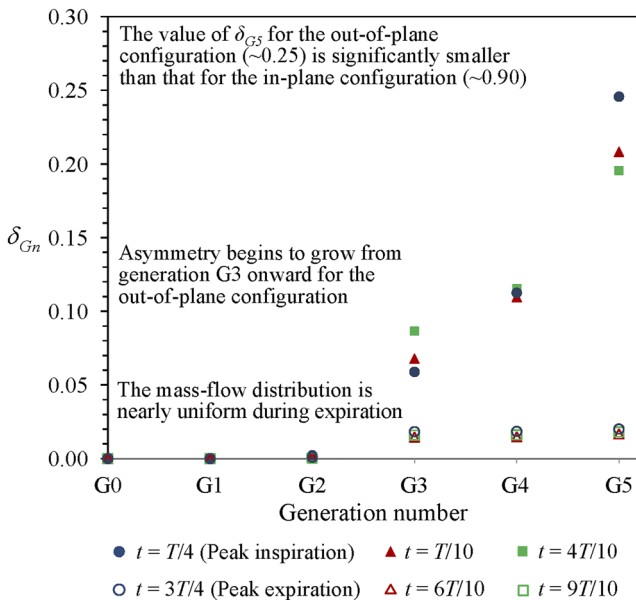


FIG. 29. Spatial evolution of the degree of mass-flow asymmetry with increasing generation number at various instants of the breathing cycle; out-of-plane configuration.

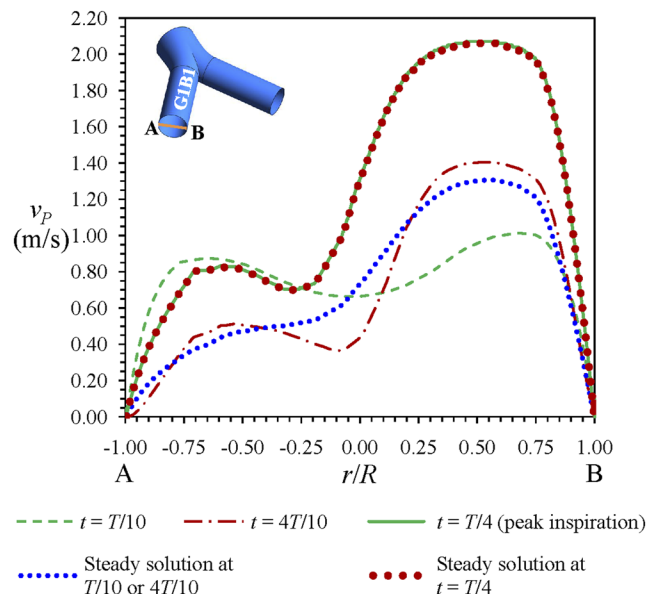


FIG. 30. Variation of the primary velocity at plane G1P1 along the diameter AB which lies on the meridional plane at different time instants during the inspiratory phase for $\alpha_{G0} = 10$; in-plane configuration.

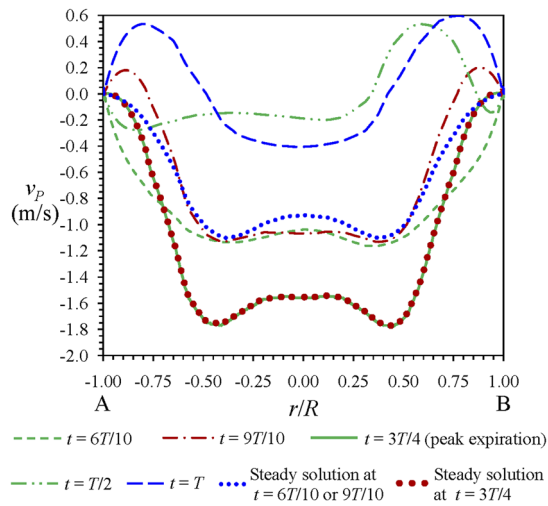


FIG. 31. Variation of the primary velocity at plane G1P1 along the diameter AB which lies on the meridional plane during the expiratory phase and at instants of changeover ($t = T/2, t = T$) for $\alpha_{G0} = 10$; in-plane configuration.

solutions. Moreover, bidirectional flow is observed at $t = 9T/10$ (Fig. 31) whereas flow at the same time instant is unidirectional at the lower value of the Womersley number (Fig. 22). Thus, it is concluded that bidirectional flow exists over greater portion of a cycle as the Womersley number is increased. However, similar to the trends at $\alpha_{G0} = 2.64$, the unsteady effects during the inspiratory phase (Fig. 30) are greater than that during the expiratory phase (Fig. 31) at $\alpha_{G0} = 10$. This considerable difference in the unsteady effects during inspiration and that during expiration, which is peculiar to the branching network, destroys the temporal symmetry of the solution prevalent in oscillating pipe flows.

Figure 31 also shows the unsteady solutions at $t = T/2$ and at $t = T$. As explained previously, the flow at these time instants are solely due to the unsteady effects. As in the case of $\alpha_{G0} = 2.64$, bidirectional flow is observed at $\alpha_{G0} = 10$. However, a comparison of Figs. 31 and 22 shows that the magnitudes of the primary velocity are greatly increased at $\alpha_{G0} = 10$, and the velocity distribution at $t = T/2$ is highly asymmetric with respect to the radius. Even the velocity distribution at $t = T$ shows more asymmetry with respect to radius as compared to that observed at $\alpha_{G0} = 2.64$. Thus, the increase of the Womersley number leads to a considerable increase of flow velocities and asymmetries during changeover from inspiration to expiration and vice-versa, where the unsteady effects are at their maximum.

In Figs. 32 and 33, we have plotted the primary velocity contours and secondary flow patterns at selected cross sections in the branching network at those time instants of the cycle where the unsteady effects are maximum (i.e., at $t = T/2$ and $t = T$). As explained previously, the nonuniform flow structure seen in Figs. 32 and 33 is entirely due to the unsteady effects since a steady flow solution with the same boundary condition would have resulted in zero velocity everywhere in the flow field. The basic flow features—viz., the presence of bidirectional primary flow, progressive decrease of the range of velocity magnitude from G0 to G3, and secondary flow patterns similar to those occurring in the respective preceding parts of the cycle—are similar to those observed at $\alpha_{G0} = 2.64$ (Figs. 6, 8, 14, and 16). However, it is found that the range of primary velocity magnitude (negative to positive) at $\alpha_{G0} = 10$ is significantly greater than that at $\alpha_{G0} = 2.64$. As the Womersley number at G0 is increased from 2.64 to 10, the Womersley number at generation G3 also increases and this is reflected in the presence of considerable velocities even at generation G3. The magnitudes of average secondary velocity $\bar{v}_s (\equiv \sqrt{\int |\vec{v}_s|^2 dA/\pi R^2})$ at time instants $t = T/2$ and $t = T$ for the Womersley number

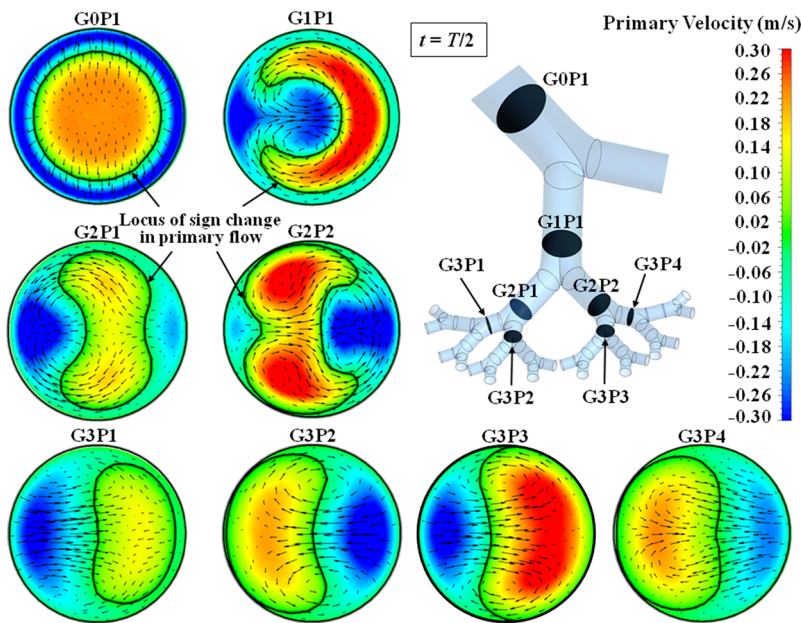


FIG. 32. Distribution of primary and secondary velocities at the specified planes in branches of generations G0-G3 at the end of inspiration ($t = T/2$) for $\alpha_{G0} = 10$; in-plane configuration.

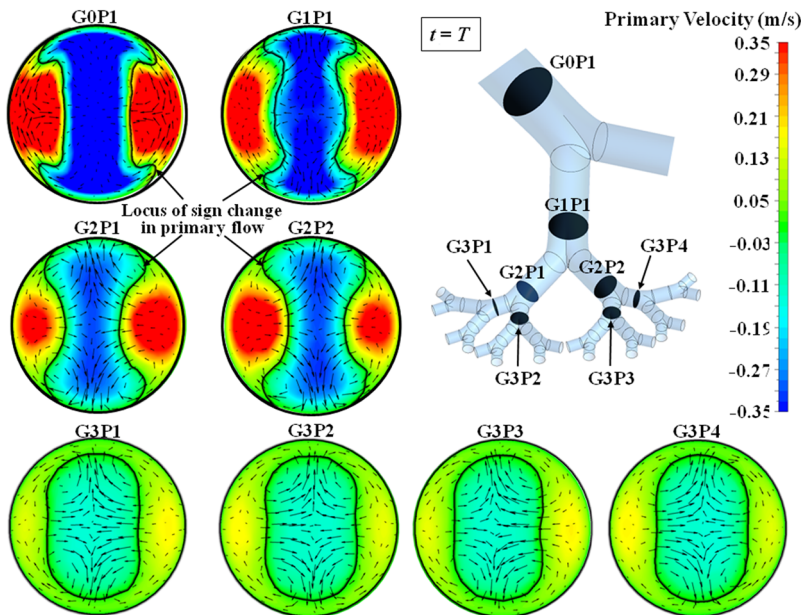


FIG. 33. Distribution of primary and secondary velocities at the specified planes in branches of generations G0-G3 at the end of expiration ($t = T$) for $\alpha_{G0} = 10$; in-plane configuration.

$\alpha_{G0} = 10$ are also considerably greater than the corresponding values for $\alpha_{G0} = 2.64$.

Figure 34 shows the inter-relationships between the prescribed oscillation in velocity (V_{G0S1}) and the oscillation in computed static pressure drop (Δp) across the branching network at two values of the Womersley number. It is interesting to note that the two curves for Δp intersect approximately at peak inspiration (maximum point in the velocity curve) and at peak expiration (negative maximum in the velocity curve). We have already shown that at these two points there is negligible difference between the respective unsteady solution and steady solution. By virtue of using the same Re_{max} for both

simulations shown in Fig. 34, the corresponding steady solutions are the same. This explains why the Δp curves for different values of α_{G0} are intersecting approximately at the points of peak inspiration and peak expiration.

When we constructed the equivalent of Fig. 23 at $\alpha_{G0} = 10$, we found that the figure remained almost the same. We thus conclude that, for the same maximum inlet Reynolds number, the time variation of the average velocity through any branch (\bar{V}_{branch}) is almost independent of the Womersley number α_{G0} . Figure 34, on the other hand, shows that, for the same $V_{G0S1}(t)$, both the amplitude and the phase difference of the oscillation in static pressure drop across the network, $\Delta p(t)$, increase with increasing α_{G0} . The oscillations in velocity and pressure bear similar qualitative inter-relationships in the analytical formulation of Womersley¹⁸ for the oscillating flow in a pipe. Analytical formulae, however, are not available for an elaborate 3D branching network, and the inter-relationships have to be determined either by performing experiments or by conducting CFD simulations as is done here.

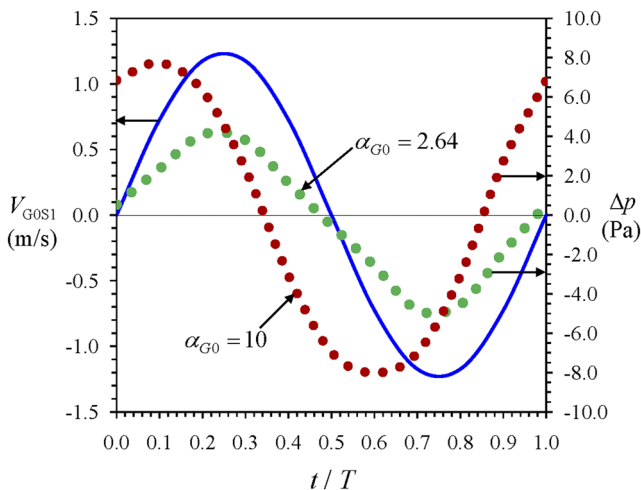


FIG. 34. Inter-relationships between the prescribed oscillation in velocity and the oscillation in computed static pressure drop across the branching network at two values of Womersley number.

V. CONCLUSION

The present computational study attempts to capture the complex fluid dynamics associated with the oscillatory flow in three-dimensional branching networks, involving periodic reversal of the predominant flow direction, through accurate unsteady simulations of the flow field (with experimental validation of both steady and unsteady computational results). The geometry of the network adopted here is based on the first six generations of a model human bronchial tree comprising 63 straight sections and 31 bifurcation modules. The task is therefore computationally challenging. Spatial and temporal accuracy of the solution is demonstrated so that dependable physical conclusions can be made from the simulations presented. A visual appreciation of the spatial and temporal evolutions of the three-dimensional velocity field may be

obtained in Figs. 9–12 for in-plane and Figs. 17–20 for out-of-plane configurations, contrasting the fluid dynamics in the inspiratory and expiratory phases and displaying the effects of three-dimensional arrangement of the same branches on the oscillatory flow structures. The physical understanding of the fluid dynamics of steady expiratory flow through an elaborate branching network is taken to a similar level of fine details that have been previously established for steady inspiratory flow in Refs. 1 and 2. The nature of the unsteady effects is thoroughly discussed in Secs. IV B and IV E. Although computations are carried out here for a model bronchial tree, the conclusions and physical understanding emanating from this study are also applicable to oscillating flow in a future engineered branching network.

With the help of the present unsteady simulations, the validity of the frequently used quasisteady assumption is assessed here (Figs. 21 and 22). It is established that the quasisteady assumption is approximately valid in the neighborhood of the peak flow rate, both during inspiration and expiration. However, during inspiration, significant differences in the flow field are possible between two corresponding instants of accelerating and decelerating parts. Such differences are smaller during expiration. Unsteady effects are at their maximum during the changeover from expiration to inspiration ($t = 0$ or $t = T$) and inspiration to expiration ($t = T/2$). Section IV B describes how the symmetry of the solution with respect to both space and time—found in the oscillating, fully developed flow in a pipe—are destroyed in the unsteady effects that occur in the oscillating flow in a branching network.

The effects of the Womersley number on the unsteady fluid dynamics in an elaborate branching network (see Figs. 21, 22, 30, and 31) are established here by performing simulations at two values of the Womersley number (2.64 and 10 based on the radius of generation G0), each simulation taking about 1000 h of processor time on four parallelized i-5 processors. The effects of varying the Womersley number can also be discerned from either of the two simulations since its value progressively decreases in the direction G0-G5, as the radius of the branches decreases. This is reflected, for example, in the flow solutions at $t = T/2$ and $t = T$. The prescribed volume flow rate at these time instants at the computational boundary is zero; thus, a steady flow solution would give zero velocity at every point of the computational domain. The nonuniform flow structures seen in Figs. 6, 8, 10, 12, 14, 16, 18, and 20 are thus entirely due to the unsteady effects. The progressive decrease in the amplitude of velocity variation in the direction G0-G5, as seen in the above-mentioned figures, is due to the decreasing Womersley number. A comparison of Figs. 10 and 12, and that of Figs. 18 and 20, show that at both time instants $t = T/2$ and $t = T$, bidirectional flow with almost equal magnitude of velocities in both directions (with significant secondary motion at a cross section) exists, but there are differences in the details of the velocity distribution. During the changeover from expiration to inspiration ($t = 0$ or $t = T$), expiratory flow occurs in the central region within the closed curve, while inspiratory flow occurs in the peripheral regions. The reverse flow structure occurs during the changeover from inspiration to expiration ($t = T/2$). At $t = T/2$, one inspiratory peak and one expiratory peak are observed at a cross section. At $t = T$, two expiratory peaks and two inspiratory peaks are observed, though all peaks are not well-defined. This difference is the manifestation of different degrees of cross-sectional flow asymmetry developed in the

respective preceding part of the cycle. As the Womersley number is increased, the unsteady effects at all branches increase, and bidirectional flow exists over greater portion of a cycle. However, the time-variation of the average velocity through any branch is found not to depend on the Womersley number (for the fixed inlet Reynolds number).

Significant differences are observed between the velocity fields during inspiration and expiration (in both configurations), even though the magnitudes of average velocity at the start-plane of G0B1 (at each corresponding phase) are equal. The velocity distributions in most of the branches show a single peak during inspiration, with that peak located near the wall aligned with the inner edge of the preceding bifurcation (Figs. 5, 9, 13, and 17). During expiration, the cross-sectional velocity distribution for the in-plane configuration (Fig. 11) is characterized by four centrally located peaks at the beginning (GnP_k) of the straight section of a branch, with the peaks tending to merge along the straight length to give a plateaulike velocity distribution toward the end ($GnSk$) of the straight section. On the other hand, for the out-of-plane configuration (Fig. 19), the cross-sectional velocity distribution during expiratory flow is characterized by four peaks in G0, four in G1, two peaks (though not well-defined) in G2, followed by a single peak in generation G3 onward.

The secondary flow field in both configurations at peak inspiration and peak expiration show qualitatively similar characteristics to their steady-state counterparts. While the secondary velocity distribution during peak inspiration is similar for the two configurations up to the plane G1P1, the effect of the three-dimensional arrangement becomes appreciable from generation G2 onward. On the other hand, during peak expiration, the secondary velocity distributions are different for the two configurations in all generations. Owing to the more tortuous flow path, the strength of secondary flow in the out-of-plane configuration (Fig. 25) is greater than that in the in-plane configuration (Fig. 24). While this is true for all generations at peak expiration, the secondary flow strength at peak inspiration is similar for the two configurations up to plane G1P1 due to identical flow paths from the inlet up to that plane. At peak inspiration, a bifurcation module alters the qualitative nature of the secondary flow pattern and increases secondary flow strength, and the straight portion of a branch only attenuates secondary flow strength without affecting the vortex pattern. On the other hand, during expiration, changes in the vortex pattern occur in the straight portion of a branch, and flow recombination at a bifurcation module regenerates vortical secondary motion.

The flow field during inspiration for the in-plane configuration is highly asymmetric with nonuniform mass flow distribution among the branches of a generation even though the adopted branching network is geometrically symmetric. The asymmetry in the mass flow distribution during inspiration is significantly lower for the out-of-plane configuration as compared to its in-plane counterpart. The degree of mass-flow asymmetry during expiration is about an order of magnitude smaller than that during inspiration for both configurations. It is concluded that since a bifurcation module gives rise to flow division during the inspiratory phase, it consequently generates nonuniformity in the flow distribution, whereas in the same bifurcation module combination of fluid streams takes place during the expiratory phase, thereby tending to enhance

symmetry in the flow field. On the other hand, flow at peak inspiration is unidirectional from G0-G5, while small regions of oppositely directed flow (i.e., inspiratory flow) of small magnitude are seen to occur near the walls during peak expiration in generations G0-G2. Even though the magnitude of prescribed volume flow rate at the computational boundary is the same at $t = T/4$ and $t = 3T/4$, the stunning visual difference between the flow structures at the two instants on the meridional plane (shown in Fig. 26) and on the cross-sectional planes (Fig. 5 vs Fig. 7, Fig. 13 vs Figs. 15, 24, and 25) vividly demonstrates the fundamental difference between a successively bifurcating flow and a successively combinatory flow, illustrating the essential irreversibility of fluid dynamics.

ACKNOWLEDGMENTS

The authors express their gratitude to the (anonymous) referees for their appreciation that has inspired the authors and for their constructive suggestions that have improved the clarity of the paper.

REFERENCES

- ¹A. Guha, K. Pradhan, and P. K. Halder, "Finding order in complexity: A study of the fluid dynamics in a three-dimensional branching network," *Phys. Fluids* **28**(12), 123602 (2016).
- ²A. Guha and K. Pradhan, "Secondary motion in three-dimensional branching networks," *Phys. Fluids* **29**(6), 063602 (2017).
- ³Y. Zhao and B. B. Lieber, "Steady inspiratory flow in a model symmetric bifurcation," *J. Biomech. Eng.* **116**(4), 488–496 (1994).
- ⁴Y. Zhao and B. B. Lieber, "Steady expiratory flow in a model symmetric bifurcation," *J. Biomech. Eng.* **116**(3), 318–323 (1994).
- ⁵M. Y. Kang, J. Hwang, and J. W. Lee, "Effect of geometric variations on pressure loss for a model bifurcation of the human lung airway," *J. Biomech.* **44**(6), 1196–1199 (2011).
- ⁶J. K. Comer, C. Kleinstreuer, and Z. Zhang, "Flow structures and particle deposition patterns in double-bifurcation airway models. Part 1. Air flow fields," *J. Fluid Mech.* **435**, 25–54 (2001).
- ⁷F. Wilquem and G. Degrez, "Numerical modeling of steady inspiratory airflow through a three-generation model of the human central airways," *J. Biomech. Eng.* **119**(1), 59–65 (1997).
- ⁸Z. Zhang, C. Kleinstreuer, and C. S. Kim, "Flow structure and particle transport in a triple bifurcation airway model," *J. Fluids Eng.* **123**(2), 320–330 (2001).
- ⁹H. Y. Luo and Y. Liu, "Modeling the bifurcating flow in a CT-scanned human lung airway," *J. Biomech.* **41**(12), 2681–2688 (2008).
- ¹⁰O. Pourmehran, T. B. Gorji, and M. Gorji-Bandpy, "Magnetic drug targeting through a realistic model of human tracheobronchial airways using computational fluid and particle dynamics," *Biomech. Model. Mechanobiol.* **15**(5), 1355–1374 (2016).
- ¹¹M. Rahimi-Gorji, O. Pourmehran, M. Gorji-Bandpy, and T. B. Gorji, "CFD simulation of airflow behavior and particle transport and deposition in different breathing conditions through the realistic model of human airways," *J. Mol. Liq.* **209**, 121–133 (2015).
- ¹²V. Goodarzi-Ardakani, M. Taeibi-Rahni, M. R. Salimi, and G. Ahmadi, "Computational simulation of temperature and velocity distribution in human upper respiratory airway during inhalation of hot air," *Respir. Physiol. Neurobiol.* **223**, 49–58 (2016).
- ¹³A. J. Banko, F. Coletti, D. Schiavazzi, C. J. Elkins, and J. K. Eaton, "Three-dimensional inspiratory flow in the upper and central human airways," *Exp. Fluids* **56**(6), 117 (2015).
- ¹⁴A. Guha, "Transport and deposition of particles in turbulent and laminar flow," *Annu. Rev. Fluid Mech.* **40**, 311–341 (2008).
- ¹⁵T. Sxrl, "Über den von EG Richardson entdeckten, annuläreffekt," *Z. Phys.* **61**(5-6), 349–362 (1930).
- ¹⁶E. G. Richardson and E. Tyler, "The transverse velocity gradient near the mouths of pipes in which an alternating or continuous flow of air is established," *Proc. Phys. Soc.* **42**(1), 1–15 (1929).
- ¹⁷P. Lambossy, "Oscillations forces d'un liquide incompressible et visqueux dans un tube rigide et horizontal. Calcul de la force frottement," *Helv. Phys. Acta* **25**, 371–386 (1952).
- ¹⁸J. R. Womersley, "Method for the calculation of velocity, rate of flow and viscous drag in arteries when the pressure gradient is known," *J. Physiol.* **127**(3), 553–563 (1955).
- ¹⁹J. R. Womersley, "Oscillatory flow in arteries: The constrained elastic tube as a model of arterial flow and pulse transmission," *Phys. Med. Biol.* **2**(2), 178–187 (1957).
- ²⁰S. Ray and F. Durst, "Semianalytical solutions of laminar fully developed pulsating flows through ducts of arbitrary cross-sections," *Phys. Fluids* **16**(12), 4371–4385 (2004).
- ²¹G. J. Brereton and S. M. Jalil, "Diffusive heat and mass transfer in oscillatory pipe flow," *Phys. Fluids* **29**(7), 073601 (2017).
- ²²H. L. Ma and C. H. Kuo, "Theoretical analysis of an oscillatory plane Poiseuille flow—A link to the design of vortex flow meter," *Phys. Fluids* **29**(5), 053602 (2017).
- ²³A. Tsimpoukis and D. Valougeorgis, "Pulsatile pressure driven rarefied gas flow in long rectangular ducts," *Phys. Fluids* **30**(4), 047104 (2018).
- ²⁴D. L. Jan, A. H. Shapiro, and R. D. Kamm, "Some features of oscillatory flow in a model bifurcation," *J. Appl. Physiol.* **67**(1), 147–159 (1989).
- ²⁵A. S. Menon, M. E. Weber, and H. K. Chang, "Model study of flow dynamics in human central airways. Part III: Oscillatory velocity profiles," *Respir. Physiol.* **55**(2), 255–275 (1984).
- ²⁶B. B. Lieber and Y. Zhao, "Oscillatory flow in a symmetric bifurcation airway model," *Ann. Biomed. Eng.* **26**(5), 821–830 (1998).
- ²⁷F. E. Fresconi and A. K. Prasad, "Secondary velocity fields in the conducting airways of the human lung," *J. Biomech. Eng.* **129**(5), 722–732 (2007).
- ²⁸P. Evegren, L. Fuchs, and J. Revstedt, "On the secondary flow through bifurcating pipes," *Phys. Fluids* **22**(10), 103601 (2010).
- ²⁹B. Soni and D. Thompson, "Effects of temporally varying inlet conditions on flow and particle deposition in the small bronchial tubes," *Int. J. Numer. Methods Biomed. Eng.* **28**(9), 915–936 (2012).
- ³⁰Z. Zhang and C. Kleinstreuer, "Transient airflow structures and particle transport in a sequentially branching lung airway model," *Phys. Fluids* **14**(2), 862–880 (2002).
- ³¹K. Adler and C. Brücker, "Dynamic flow in a realistic model of the upper human lung airways," *Exp. Fluids* **43**(2-3), 411–423 (2007).
- ³²M. A. Nagels and J. E. Cater, "Large eddy simulation of high frequency oscillating flow in an asymmetric branching airway model," *Med. Eng. Phys.* **31**(9), 1148–1153 (2009).
- ³³P. Balogh and P. Bagchi, "Analysis of red blood cell partitioning at bifurcations in simulated microvascular networks," *Phys. Fluids* **30**(5), 051902 (2018).
- ³⁴E. Kaliviotis, J. M. Sherwood, and S. Balabani, "Local viscosity distribution in bifurcating microfluidic blood flows," *Phys. Fluids* **30**(3), 030706 (2018).
- ³⁵E. R. Weibel, *Morphometry of the Human Lung* (Springer, Berlin, Heidelberg, 1963).
- ³⁶SolidWorks, Release 2010, Dassault Systèmes SolidWorks Corporation, Waltham, MA.
- ³⁷ANSYS Academic Research, Release 15.0, ANSYS, Inc. Canonsburg, PA.
- ³⁸N. Nowak, P. P. Kakade, and A. V. Annappagada, "Computational fluid dynamics simulation of airflow and aerosol deposition in human lungs," *Ann. Biomed. Eng.* **31**(4), 374–390 (2003).
- ³⁹P. W. Longest and S. Vinchurkar, "Effects of mesh style and grid convergence on particle deposition in bifurcating airway models with comparisons to experimental data," *Med. Eng. Phys.* **29**(3), 350–366 (2007).
- ⁴⁰T. Heistracher and W. Hofmann, "Flow and deposition patterns in successive airway bifurcations," *Ann. Occup. Hyg.* **41**, 537–542 (1997).

- ⁴¹T. J. Barth and D. C. Jespersen, "The design and application of upwind schemes on unstructured meshes," AIAA Paper No. 89-0366, 1989.
- ⁴²Y. Mei and A. Guha, "Implicit numerical simulation of transonic flow through turbine cascades on unstructured grids," *Proc. Inst. Mech. Eng., Part A* **219**(1), 35–47 (2005).
- ⁴³C. Kleinstreuer and Z. Zhang, "An adjustable triple-bifurcation unit model for air-particle flow simulations in human tracheobronchial airways," *J. Biomech. Eng.* **131**(2), 021007 (2009).
- ⁴⁴X. L. Yang, Y. Liu, and H. Y. Luo, "Respiratory flow in obstructed airways," *J. Biomech.* **39**(15), 2743–2751 (2006).
- ⁴⁵B. Soni, C. Lindley, and D. Thompson, "The combined effects of non-planarity and asymmetry on primary and secondary flows in the small bronchial tubes," *Int. J. Numer. Methods Fluids* **59**(2), 117–146 (2009).
- ⁴⁶A. Guha and J. B. Young, "Time-marching prediction of unsteady condensation phenomena due to supercritical heat addition," in *Turbomachinery: Latest Developments in a Changing Scene* (Institution of Mechanical Engineers, London, UK, 1991), ISBN: 0852987617, pp. 167–177.
- ⁴⁷A. Guha, "Thermal choking due to nonequilibrium condensation," *J. Fluids Eng.* **116**(3), 599–604 (1994).
- ⁴⁸P. J. Roache, "Quantification of uncertainty in computational fluid dynamics," *Annu. Rev. Fluid Mech.* **29**(1), 123–160 (1997).
- ⁴⁹I. B. Celik, U. Ghia, and P. J. Roache, "Procedure for estimation and reporting of uncertainty due to discretization in CFD applications," *J. Fluids Eng.* **130**(7), 078001 (2008).
- ⁵⁰K. Avila, D. Moxey, A. de Lozar, M. Avila, D. Barkley, and B. Hof, "The onset of turbulence in pipe flow," *Science* **333**(6039), 192–196 (2011).
- ⁵¹J. Jeong and F. Hussain, "On the identification of a vortex," *J. Fluid Mech.* **285**, 69–94 (1995).
- ⁵²A. Guha and S. Sengupta, "The fluid dynamics of work transfer in the non-uniform viscous rotating flow within a Tesla disc turbomachine," *Phys. Fluids* **26**(3), 033601 (2014).
- ⁵³S. Sengupta and A. Guha, "The fluid dynamics of symmetry and momentum transfer in microchannels within co-rotating discs with discrete multiple inflows," *Phys. Fluids* **29**(9), 093604 (2017).